The Abdus Salam
International Centre for Theoretical Physics

United Nations
Educational, Scientific and
Cultural Organization

IAEA
International Atomic Energy Agency

1965-4

9th Workshop on Three-Dimensional Modelling of Seismic Waves Generation, Propagation and their Inversion

22 September - 4 October, 2008

Surface Wave Tomography and Inversion for 3D Shear Velocity Model

A.L. Levshin
University of Colorado, Boulder, U.S.A.

---

levshin@anquetil.colorado.edu

A. L. Levshin

University of Colorado, Boulder, U.S.A.

Surface Wave Tomography and Inversion for 3D Shear Velocity Model

The relation between surface-wave dispersion and the seismic velocity structure of the earth is nonlinear. There are two common approaches to resolve this nonlinearity in the inverse problem. One is waveform fitting in which the relation between the model and the seismic waveforms is linearized and the model is iteratively estimated (e.g., Snieder (1988), Nolet (1990,2008), Marquering (1996)). Our approach, in contrast, is based on direct measurements of surface wave dispersion rather than fitting waveforms so that the nonlinear inverse problem is divided into two steps: (1) a nearly linear part that we call surface wave tomography to estimate 2-D dispersion maps and (2) a nonlinear inversion of the dispersion curves at each geographical point for a shear velocity model of the crust and upper mantle. Our tomographic studies in the Center for Imaging the Earth's Interior, University of Colorado at Boulder (CU-B), USA, have different scales: global and regional. I will show some results of the global and regional tomography.

Step 1. Surface wave tomography

1.1. Measurements

We measure the group velocities using frequency-time analysis (FTAN) (Levshin *et al.*, 1989) described in the previous lecture.

Global tomography

For global tomography we used broadband waveforms following earthquakes that occurred from 1977 - 2002 at stations from both global networks (GDSN, GSN, GEOSCOPE, GEOFON), regional arrays (MEDNET, Canadian Network, KNET, KAZNET, POSEIDON) as well as temporary regional arrays (e.g., Saudi Arabian Network, SKIPPY in Australia, PASSCAL deployments in Tibet, South America, Antarctica, and South Africa). The phase velocities were measured at Harvard University and Utrecht University, separately. These phase velocity data sets are described by Ekström (1997) and Trampert & Woodhouse (1995). We merged all phase velocity measurements into a single data set. A cluster analysis, i.e. combining many similar paths into one "common" path, is applied to both the group and phase velocity measurements for out-lier rejection and rms estimation. The results of this analysis show that typical measurement errors are 20 - 25 m/s for group velocities, except for very short periods, and 10 - 15 m/s for phase velocities, except for long period Love waves.

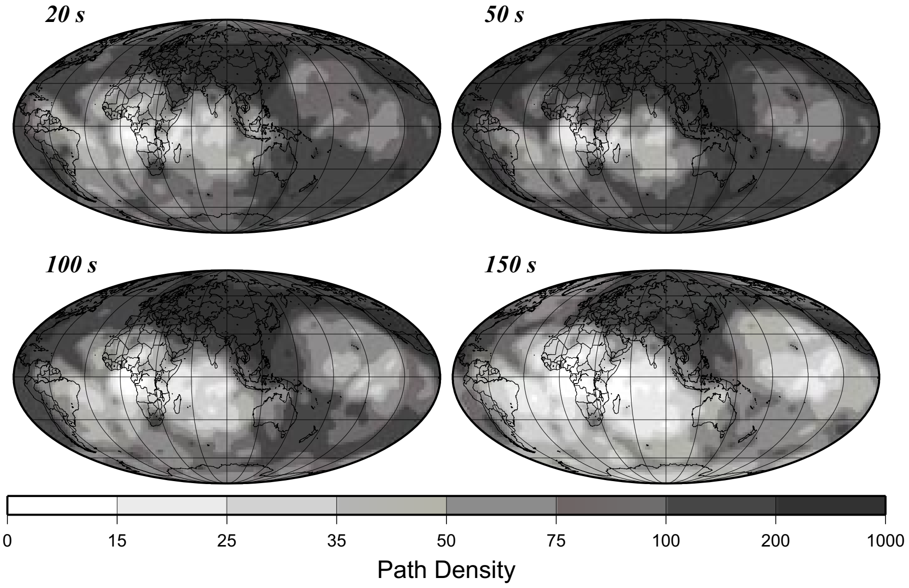

Figure 1: Examples of path density.

Data coverage is generally better for Rayleigh waves than for Love waves, is better at intermediate than at very short or very long periods, and is better in the northern than in the southern hemisphere. This heterogeneous data coverage is imposed by the distribution of receiving stations and earthquakes. Data coverage optimizes in Eurasia and is currently worst across Africa, the central Pacific, parts of the Indian Ocean, and Antarctica. The whole data set consists of more than 100,000 group velocity paths and 50,000 phase velocity paths. Figure 1 presents examples of path coverage. Path density there is defined as a number of paths crossing the cell $2^o \times 2^o$.

Regional tomography

As an example of the regional tomography I will show results of the recent work of a joint team: CU-B, NORSAR, and University of Oslo on the crustal-upper mantle structure of the Barents Sea (Levshin *et al.*, 2006) To improve the data coverage in the target region, we have extensively searched for long period and broadband data from seismic stations and arrays in the European Arctic, including local networks and temporary array installments. We were able to retrieve surface waveform data and make surface wave dispersion observations on data from archives at NORSAR, University of Bergen, the Kola Science Center in Apatity, the Geological Survey of Denmark and the University of Helsinki, in addition to data retrievable from the international data centres at IRIS and GEOFON. An overview map of the station locations is in Fig. 2 (top). New Love- and Rayleigh-wave data were identified for more than 150 seismic events (including 25 nuclear tests at Novaya Zemlya and 13 so-called Peaceful Nuclear Explosions (PNEs) within the former Soviet Union) spanning a time period from 1971 to 2005. Fig. 2 (bottom) shows the geographic distribution of these events. The PNE have not been used previously for surface wave studies.

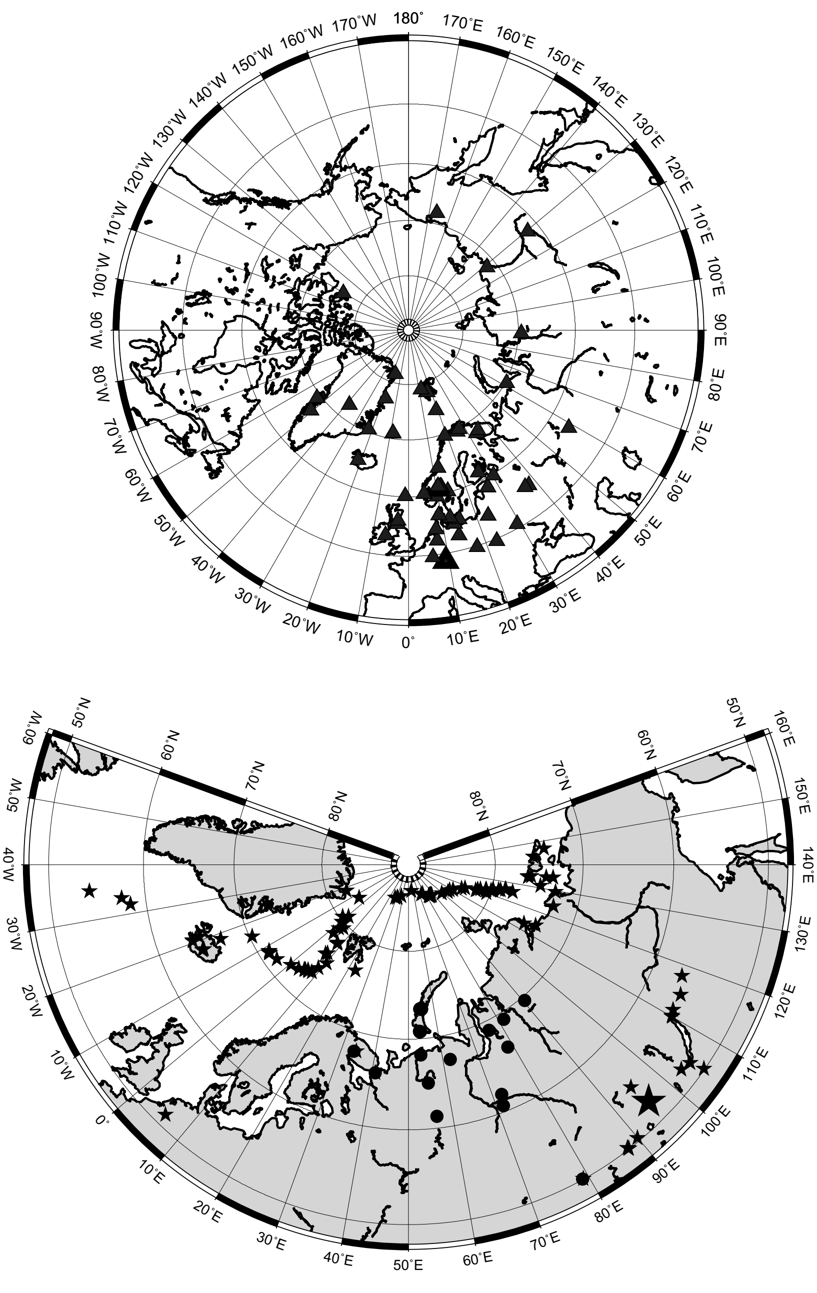

Figure 2: The top map shows the location of the seismic stations from which in the study data were retrieved. The map at the bottom shows the distribution of seismic events from which surface data were analyzed in this study. The epicenters of the earthquakes are shown by stars and of the explosions by black circles.

1.2 Surface wave tomography

In the first step, the processed group and phase velocity dispersion measurements for each wave type (Rayleigh, Love) and period are converted to 2-D dispersion maps. We construct maps on a $2^\circ \times 2^\circ$ grid world-wide in the following period bands: group velocity, 16 - 200 s; phase velocity, 40 - 150 s. These maps typically fit the measured group velocities with rms misfits of 40 - 50 m/s and the measured phase velocities to 20 - 40 m/s, or about twice the measurement error.

Historically we used two methods for tomographic inversion.
Both methods are based on a grid representation of the earth model and triangular interpolation between grid points. Both methods try to minimize the difference between observed and predicted by the model travel times along epicenter-station paths. Both methods start search from a reference model and include damping and regularization as well as special constraints for zones of the map poorly covered by observations. The difference between methods is in the definition of surface wave rays. The first method which we call "**Gaussian Tomography**" defines the ray as a stripe on a sphere centered around the great circle paths with the sensitivity to the structure decreasing with the distance d from the central ray as $exp(-d^2/2\sigma^2)$ (Figure 3). We use values of σ that vary with period and wave type from $\sim$ 200 to 350 km, so the full-width of the ray at 10% of the maximum amplitude is about 6σ; i.e., it varies from about 1200 to 2100 km from short to long periods.

However, this is a crude approximation to the real scattering of the wave which is epicentral distance and period depending. To make it more realistic it is necessary to introduce the estimates of ray sensitivity based on scattering theory. The simplest way to do it is to estimate the width of the first Fresnel zone along the ray of given period. We call this tomographic technique "**Diffraction Tomography**". The region over which surface waves scatter is defined by an ellipse on a sphere given by the the equation

$$|\Delta - (\Delta_1 + \Delta_2)| = \lambda/N, \tag{1}$$

as shown in Figure 3, where λ is the wavelength of the wave of interest determined from PREM (Dziewonski & Anderson, 1981). The first Fresnel-zone encompasses all scatterers whose combined distance from the source and receiver is less than half a wavelength. This corresponds to all signals that will arrive within half a period of the first arrival, and in this case $N = 2$. The width of this zone increases as the source-receiver geodetic distance grows.

The optimal value of N to model the scattering sensitivity of surface waves on a sphere remains the subject of debate. Yoshizawa & Kennett (2002) argue that the primary "zone of influence" spans only about one-third of the width of the first Fresnel-zone, so $N = 18$ is the value that should be used in surface wave tomography. Spetzler *et al.* (2001) argue that $N = 8/3$ is the value that is consistent with the Born/Rytov approximation. To retain consistency with the Born/Rytov approximation we will use $N = 8/3$ here. We will refer to the region so defined as the "sensitivity-zone", which is a subset of the first Fresnel-zone. Sensitivity-zone widths, irrespective of the choice of N, grow with period and path length, as illustrated by Figure 4. Professor G. Nolet will describe more general approach to construction of sensitivity kernels and corresponding tomographic technique.

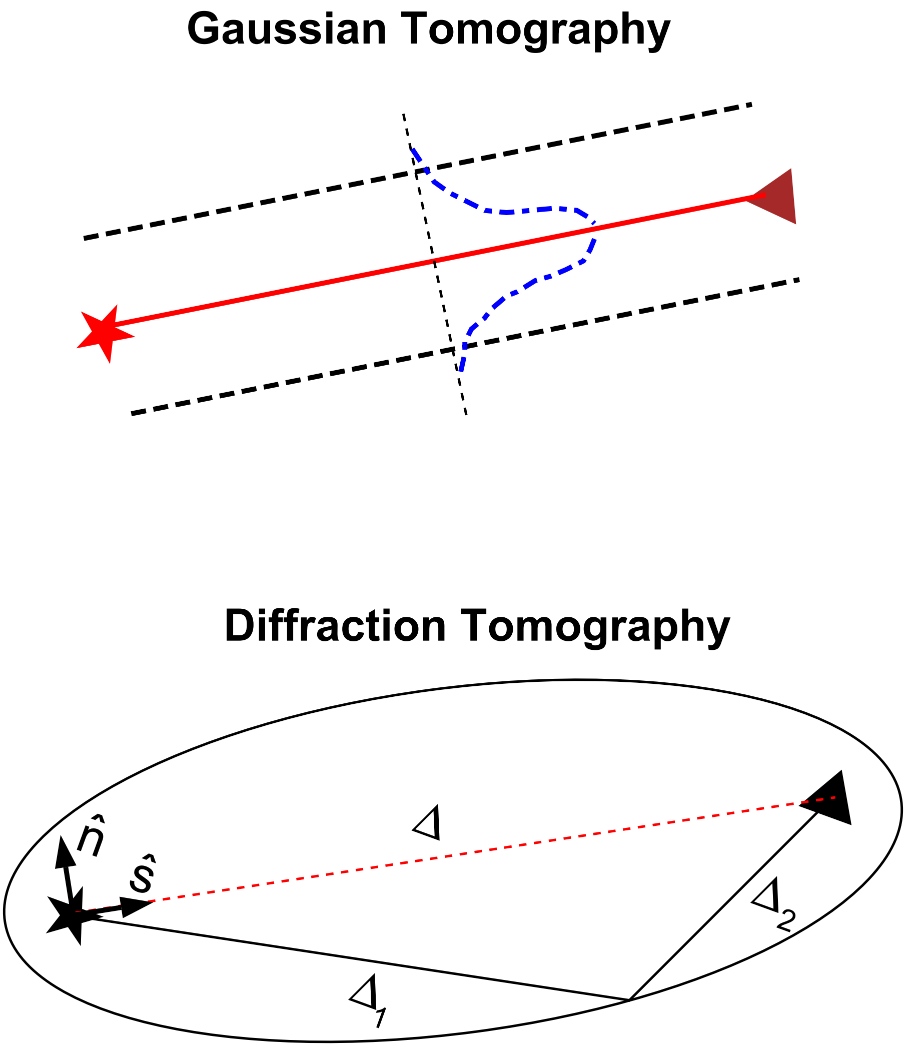

Figure 3: Schema explaining two tomographic techniques

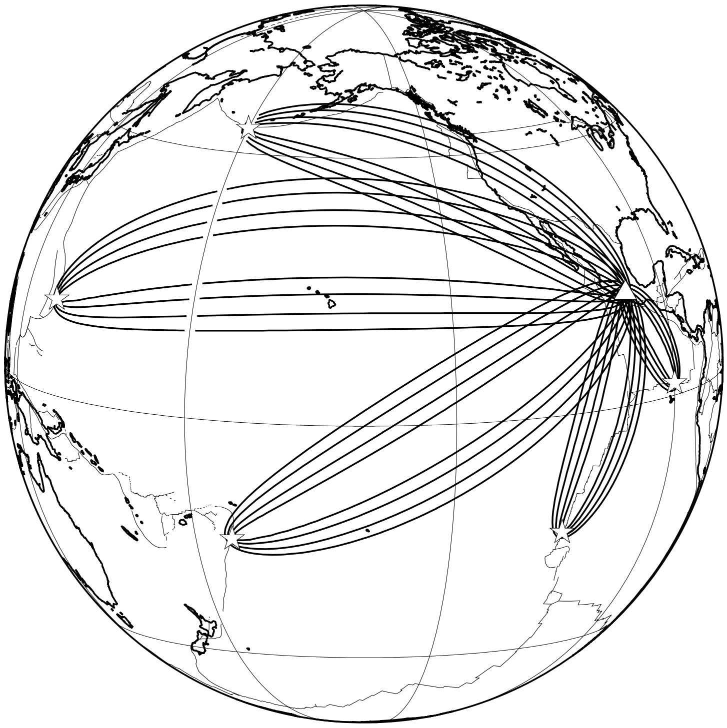

Figure 4: Rayleigh wave sensitivity-zones ($N = 8/3$) for waves observed in Mexico (triangle) originating from several epicentral regions (stars): Galapagos (2087 km), East Pacific Rise (4493 km), Aleutians (7777 km), Tonga (8916 km), and the Marianas (11700 km). These sensitivity-zones are for 20 s, 50 s, 100 s, and 150 s Rayleigh waves, where the zone is narrowest at shortest period.

The detailed description of the first method is given in Barmin *et al.* (2001), and of the second method in Ritzwoller *et al.*, (2002). Examples of group velocity maps are shown in Figure 5.

Step 2. The inversion of the tomographic maps for a shear velocity model

This inversion is a multi-stage process that culminates in a Monte-Carlo inversion for an ensemble of acceptable models at each spatial node. The middle of the ensemble ("Median Model") together with the half-width of the corridor defined by the ensemble summarize the results of the inversion. The most robust features of the resulting model are those that appear in every acceptable model. We refer to these features as "persistent" and identify them as the features of the model that are most worthy of interpretation. In regions of poor data coverage the tomographic maps and the median shear velocity model will revert to a common reference (the "Initial Model" defined below) while the uncertainties will grow up to limits imposed by a-priori constraint.

2.1. Data for Inversion

The data are surface wave group and phase velocities. Although phase ($C = \omega/k$) and group ($U = d\omega/dk$) velocities are simply related by

$$U(\omega) = \frac{C(\omega)}{1 - \dfrac{\omega}{C(\omega)}\dfrac{dC}{d\omega}} \tag{2}$$

the simultaneous inversion of U and C is substantially better than the use of either alone, as Figure 6 suggests. There are two reasons for this. First, the group velocity measurements extend to much shorter periods than the phase velocities and, therefore, provide unique constraints on shallow structures that help to resolve the trade-off between crustal and mantle structures in the inversion. This effect is amplified by the fact that group velocities are sensitive to shallower structures than phase velocities at a given period. Second, phase and group velocities are measured differently. Group velocities are measured on the amplitude of the surface wave packet and phase velocities on the phase, so the error processes in the measurements are largely independent.

2.2. Forward problem

The whole forward problem, i.e., the prediction of the surface-wave frequency dependent travel times from the three-dimensional shear-velocity model, is divided in two steps. The

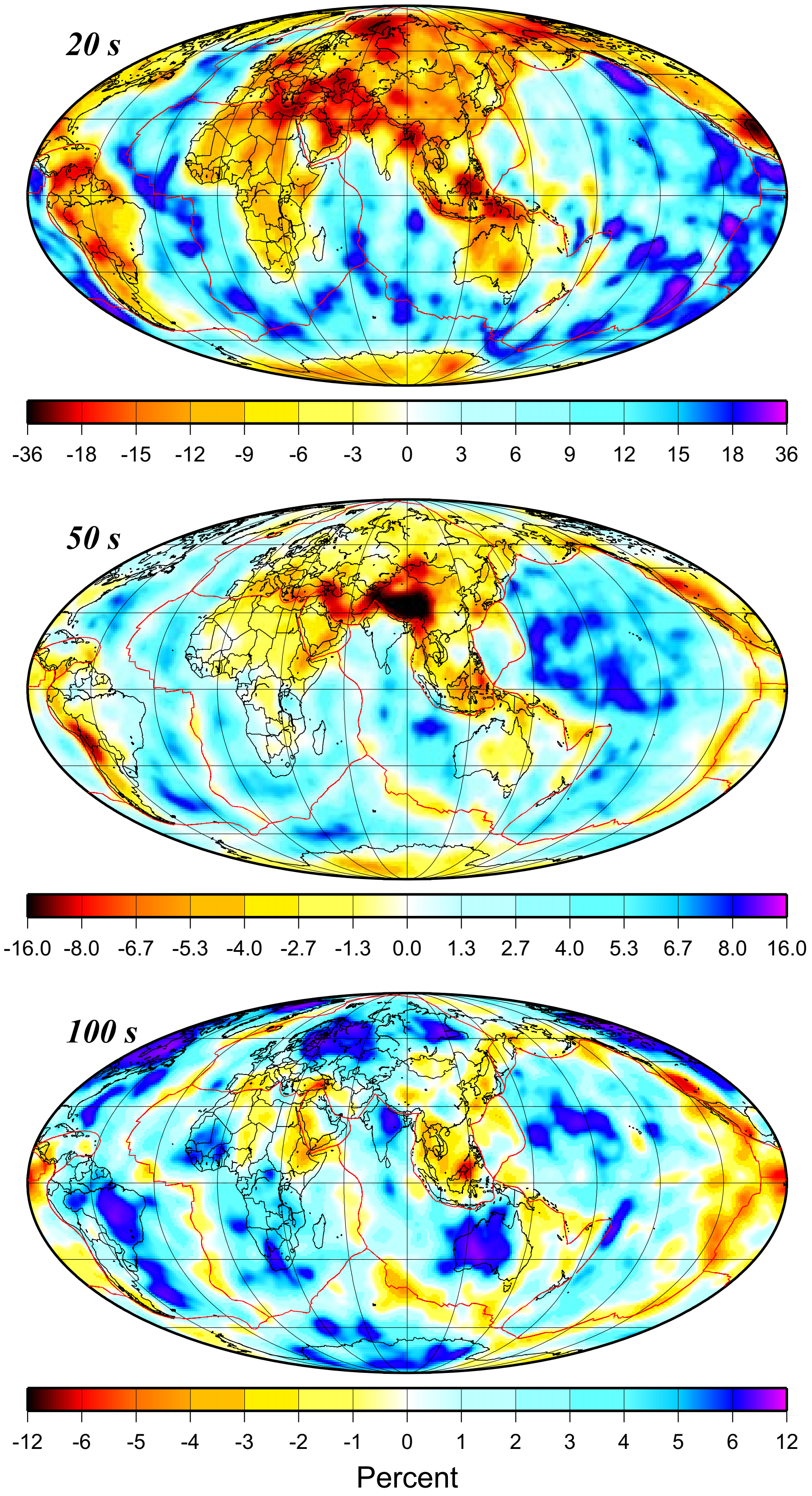

Figure 5: Examples of Rayleigh wave group velocity dispersion maps on a global scale.

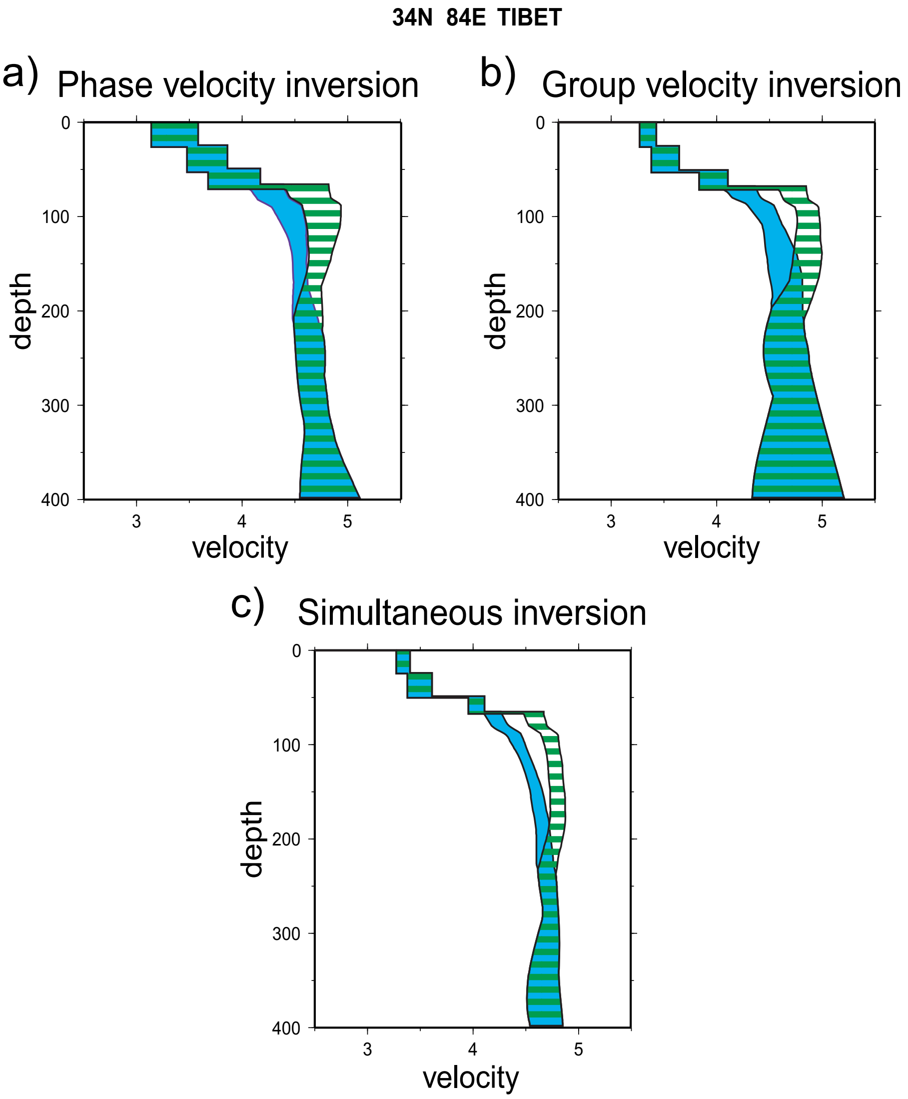

Figure 6: Examples of inversions at a point located in Tibet illustrating the relative importance of phase and group velocities: (a) inversion of the phase velocities only, (b) inversion of the group velocities only, (c) inversion of the whole data-set. The corridor of accepted SV velocities is plotted in gray and for SH velocities with horizontal hatching.

first step is the prediction of the Rayleigh and Love wave dispersion curves at each geographical points. The second step is the prediction of the surface-wave travel times for different source-receiver pairs. This last step is solved either with a ray (Gaussian) approximation or with Fresnel zone (diffraction) approximation.

At each geographical point (θ, ϕ), the Rayleigh and Love wave dispersion curves extracted from the 2-D tomographic maps compose the data vector:

$$\mathbf{d} = \left(U^R(\omega), C^R(\omega), U^L(\omega), C^L(\omega)\right)^T \tag{3}$$

where ω is frequency, C is the phase velocity, U is the group velocity, and T denotes transpose. The indices R and L refer to Rayleigh and Love waves, respectively.

The dispersion curves are assumed to result from the earth model at (θ, ϕ),

$$\mathbf{m} = (c_{ijkl}(z), \rho(z), Q(z))^T \tag{4}$$

where z is the depth, $c_{ijkl}(z)$ is the elastic tensor, $\rho(z)$ is the density, and $Q(z)$ is the quality factor. The forward problem can then be written schematically as:

$$\mathbf{d} = \mathcal{F}(\mathbf{m}) \tag{5}$$

which can be solved with a number of algorithms. We use the method and computer code of Woodhouse (1988) which operates on a radially anisotropic earth model. A radially anisotropic (or transversely isotropic) medium consists of five mutually independent elastic moduli (Smith and Dahlen, 1973), $A = \rho v_{ph}^2, C = \rho v_{pv}^2, F/(A - 2L) = \eta, L = \rho v_{sv}^2$, and $N = \rho v_{sh}^2$, so that

$$\mathbf{m} = (v_{sh}(z), v_{sv}(z), v_{ph}(z), v_{pv}(z), \eta(z), \rho(z), Q(z))^T \,. \tag{6}$$

For an isotropic solid, $A = C = \kappa + 4\mu/3, N = L = \mu, F = \kappa - 2\mu/3$, and $\eta = 1$ where κ and μ are bulk modulus and rigidity, respectively.

2.3 Inversion of dispersion curves

Because $\mathcal{F}$ is a non-linear function, $\mathcal{F}^{-1}$ is not well defined. It is common to consider the Taylor Series expansion of the forward solution around a reference model $\hat{\mathbf{m}}$:

$$\mathbf{d} = \mathcal{F}(\hat{\mathbf{m}}) + \sum_i \left(\partial\mathcal{F}/\partial m_i\right)\delta m_i + \frac{1}{2}\sum_{i,j}\left(\partial^2\mathcal{F}/\partial m_i \partial m_j\right)\delta m_i \delta m_j + \mathcal{O}(\delta m^3), \tag{7}$$

where each component of the model vector is $m_i = \hat{m}_i + \delta m_i$. If one drops the nonlinear terms, the first partial derivatives form a matrix which can be inverted with regularization constraints to estimate the perturbations δm_i. Because surface wave dispersion is dominantly affected only by v_{sv} and v_{sh}, the quantities Q, ρ, v_{pv}, and v_{ph} are commonly fixed in surface wave inversions or are set to scale in some way with the estimates of v_{sv} and v_{sh}. Villaseñor *et al.* (2002) presents an example of this approach.

2.3.1 Initial Models

Global tomography The Initial Model for global inversion is based on a variety of sources of global information, including the sediment model of Laske & Masters (1997), the crustal model CRUST5.1 of Mooney *et al.* (1998), and the shear-wave velocity model of the upper mantle S20A of Ekström & Dziewonski (1998). In Eurasia, we introduced regional information, including maps of sediment and crustal thicknesses constructed by the Russian Institute of Physics of the Earth which was converted to digital form by the Cornell Digital Earth project, and a recent model of crustal thickness over part of Eurasia based on seismic profiles, which was compiled by G. Laske (personal communication). The result is a model of the crust and upper mantle that includes a water layer where appropriate, topography on the solid surface and Moho, and 3-D variations in v_s and v_p in the sediments and crystalline crust. Shear velocities in the mantle are from the isotropic part of the model S20A modified with radial anisotropy from PREM (Dziewonski & Anderson, 1981). The average of the shear velocity model has been replaced with the 1-D model AK135 (Kennet *et al.*, 1995) in order to remove the discontinuity at 220 km in PREM. Density and isotropic compressional velocity in the mantle scale with variations in v_s using $d \ln v_p / d \ln v_s = 0.5, d \ln \rho / d \ln v_s = 0.25$. Radial anistropy is introduced into the P-wave velocities by analogy with PREM and η is set to the PREM value. The Q model is also from PREM.

Regional tomography To improve the inversion with respect to that, we applied the new crustal model BARENTS50 of the Barents Sea and surrounding areas, which had been derived in a joint project by the University of Oslo, NORSAR, and the USGS (Bungum *et al.* 2005; Ritzmann *et al.* 2006). This model has detailed information on crustal thickness and sedimentary basins in the study region with a nominal resolution of 50x50 km and helps to constrain the tomographic inversion particularly in the shallow parts of the resulting inversion. We resampled the crustal model to a 1° × 1° grid and converted the P-wave velocities given by Ritzmann *et al.* (2006) to S-wave velocities applying the P-to-S velocity transformation as used in CRUST2.0 (Bassin *et al.* 2000; http://mahi.ucsd.edu/Gabi/rem.dir/crust/crust2.html). The upper crust of model BARENTS50 with its information on sedimentary coverage of the greater Barents Sea region was used as a constraint and not altered during the inversion. The parameters of the lower crust and the depth to the Mohorovičić discontinuity were initially taken from model BARENTS50, but allowed to change during the inversion. For the upper mantle part the CU-Boulder model of Shapiro & Ritzwoller (2002) was used as the initial model down to a depth of 250 km (see also
http://ciei.colorado.edu/∼nshapiro/MODEL/index.html).
Below 300 km, we applied the Harvard model J362D28 (Antolik *et al.* 2003) as input. A smooth transition was used between these two models in the depth range from 250 to 300 km.

2.3.2 Parameterization and a priori constraints

We use a uniform parameterization over the whole globe. In the initial stage, we use eight parameters in the crust and upper mantle of which we can estimate 4-5 linear combinations. We generalize the model for Monte-Carlo inversion introducing 14 parameters, seven coefficients in the crust and seven in the mantle as shown in Figure 7.

The crust consists of three layers with constant isotropic velocities. P- and S-velocities in these layers and the crustal thickness are changed during the inversion. Isotropic mantle S-wave velocity structure is parameterized with four cubic B-splines. The remaining three coefficients parameterize the radially anisotropic part of the upper mantle with two different shear velocities, v_{sh} and v_{sv}. This radially anisotropic layer is introduced to fit simultaneously long-period Rayleigh- and Love-wave dispersion curves e.g., McEvilly (1964), Dziewonski & Anderson (1981), Gaherty & Jordan (1995). We use a simplified parameterization for radial anisotropy similar to PREM (Dziewonski & Anderson, 1981) in which two of the three coefficients are the values of v_{sh} and v_{sv} in the uppermost mantle directly beneath the crust and the third coefficient is the thickness of the anisotropic layer.

Because Rayleigh waves are predominantly sensitive to v_{sv} and Love waves to v_{sh}, we have constraints on only two of the five elastic moduli that compose a radially anisotropic model. The model needs to be completed in order to solve the forward problem, however. For want of a better solution, we set η to the PREM value at each depth and compute v_{pv} and v_{ph} using a logarithmic scaling relation from v_{sv} and v_{sh}; $d\ln v_{ph}/d\ln v_{sh} = d\ln v_{pv}/d\ln v_{sv} = 0.5$. Because the surface wave velocities are only weakly dependent on compressional velocities and η in the mantle, the arbitrariness of this procedure has little affect on the results of the inversion for v_{sh} and v_{sv}. The CU-Boulder model of Shapiro & Ritzwoller (2002) was used as the initial model down to a depth of 250 km (see also http://ciei.colorado.edu/∼nshapiro/MODEL/index.html).
Below 300 km, we applied the Harvard model J362D28 (Antolik *et al.* 2003) as input. A smooth transition was used between these two models in the depth range from 250 to 300 km.

Model, density scales with v_s and Q remains fixed at the PREM value.

Not all 14 model parameters have equal freedom during the inversion. Some are explicitly constrained. We impose two simple types of explicit constraints. First, we limit the range of perturbations for some of the parameters; i.e., $\delta m_i^{min} < \delta m_i < \delta m_i^{max}$. For example, we constrain the depth of the Moho to be varied by ±5 km relative to the Initial Model. This constraint on the Moho depth reduces the trade-off between the crustal and upper-mantle velocities. Second, we impose monotonicity constraints on the velocities in the crust; i.e., crustal velocities must satisfy $m_i < m_{i+1}$ where m_i is the velocity of a layer directly overly a layer with velocity m_{i+1}. We constrain the crustal velocities and the depths of Moho and the bottom of the anisotropic mantle. There is no explicit constraint on perturbations to the mantle velocities. However, these perturbations are implicitly constrained by the selected parameterization; i.e., the use of cubic B-splines imposes a vertical smoothness constraint.

During the global inversion we have used the uniform a-priori constraints over the whole globe. However, our inversion method allows to tune these constraints for each specific region. In particular, because the oceanic crust is younger and more homogeneous than the continental crust, we plan to apply stronger constraints on the crustal parameters in the oceans. On the contrary, in the continental regions with poor level of the a-priory knowledge of the crustal structure like Africa or Antarctica we plan to allow larger variations both in

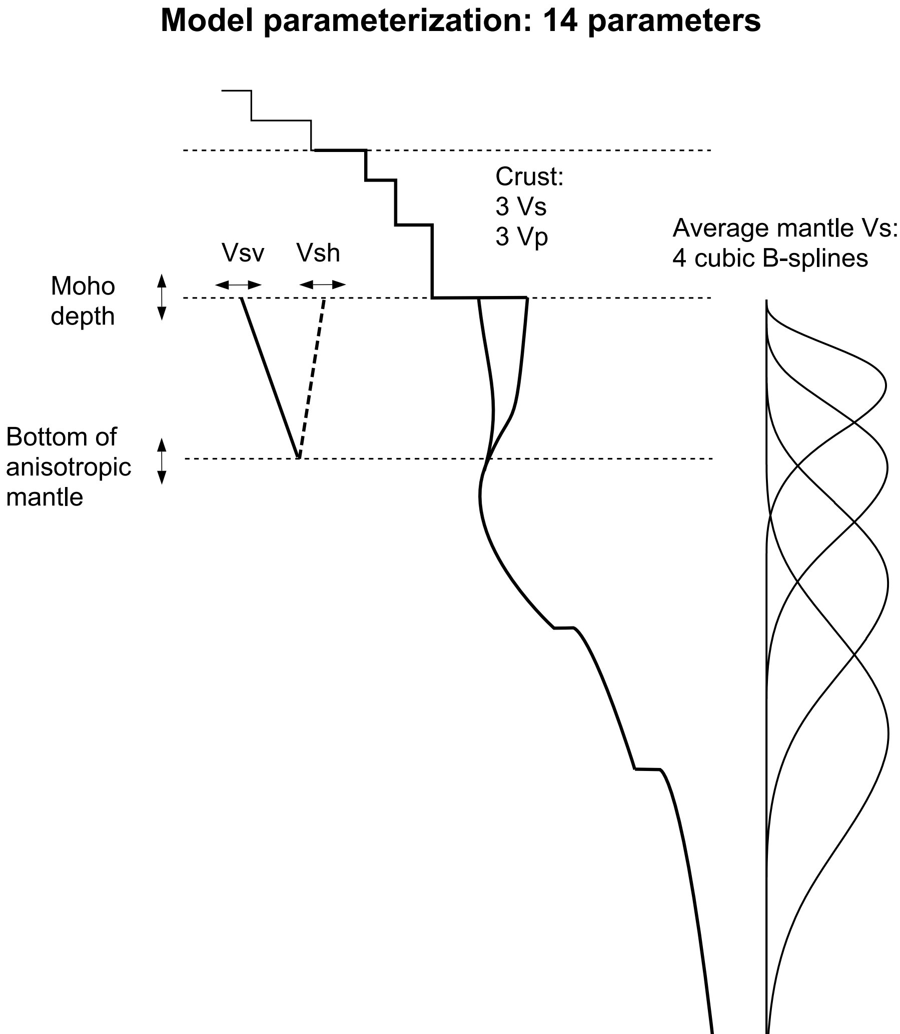

Figure 7: Model parameterization including 14 parameters: (1-3) Crustal S-wave velocities, (4-6) crustal P-wave velocities, (7) Moho depth, (8) Vsv beneath Moho, (9) Vsh beneath Moho, (10) depth of the bottom of the anisotropic mantle, (11-14) cubic B-spline perturbations to the average mantle S-wave velocity.

crustal thickness and crustal velocities.

2.3.3. Monte-Carlo inversion

I skip here the description of a preliminary step to improve the Initial Model for a given point of the grid which provides the Best Fit Model. Detailed description of this procedure is given in (Shapiro & Ritzwoller, 2002). Then we perform a Monte-Carlo (MC) sampling of the model space with an algorithm described by Shapiro *et al.* (1997). The MC inversion begins with the Best Fit Model, $\mathbf{m}^2$. The same is used as the reference model for the second-order truncated solution of the forward problem. At each MC step, the current model is randomly perturbed up to find a next model satisfying the acceptance criterion. At the following step, the random search is reinitiated in the vicinity of this new model. Therefore we call this algorithm a Brownian random walk sampling. The advantage of this technique is that it combines the speed with efficiency of the model space sampling.

In Monte-Carlo inversion, we use a cost-function defined as follows:

$$\begin{aligned} E = \sum_i W_i^{UR} \frac{|U_{obs}^R(\omega_i) - U_{pred}^R(\omega_i)|}{\sigma_i^{R,U}} + \sum_j W_j^{UL} \frac{|U_{obs}^L(\omega_j) - U_{pred}^L(\omega_j)|}{\sigma_j^{L,U}} + \\ \sum_k W_k^{CR} \frac{|C_{obs}^R(\omega_k) - C_{pred}^R(\omega_k)|}{\sigma_k^{R,C}} + \sum_l W_l^{CL} \frac{|C_{obs}^L(\omega_l) - C_{pred}^L(\omega_l)|}{\sigma_l^{L,C}} \end{aligned} \tag{8}$$

where σ denotes the estimated uncertainties in the dispersion maps and *obs* and *pred* refer to observed and predicted velocities, respectively. The L_1-norm is used for robustness to outliers. W denotes additional location-dependent weights that summarize the local quality of the dispersion maps relative to the global average. This estimate is based exclusively on the local path density of each map. In regions of poor path density, the path density weights vanish and the median model will tend to revert to the Initial Model and the uncertainty will grow up to limits imposed by a-priori constraints.

A model is considered acceptable based on the value of the cost-function for the Best Fitting Model, E_2. Typically, the acceptance criterion is $1.2E_2$; that is we accept a model if its cost (or fit) is no worse than 20% higher than the Best Fit Model. At each geographical point we test about 20,000 realizations to find an ensemble of 2,000 acceptable models. This ensemble characterizes the average properties of the structure and the uncertainty of the inversion.

2.2.4 Summarizing the ensemble of acceptable models

Results of the Monte-Carlo inversion for two points are shown in Figure 8.

The ensemble of acceptable models forms a corridor. The middle of this corridor at each depth defines the Median Model. The Median Model can be characterized in terms of perturbations relative to some global spherically symmetric model. We use the model

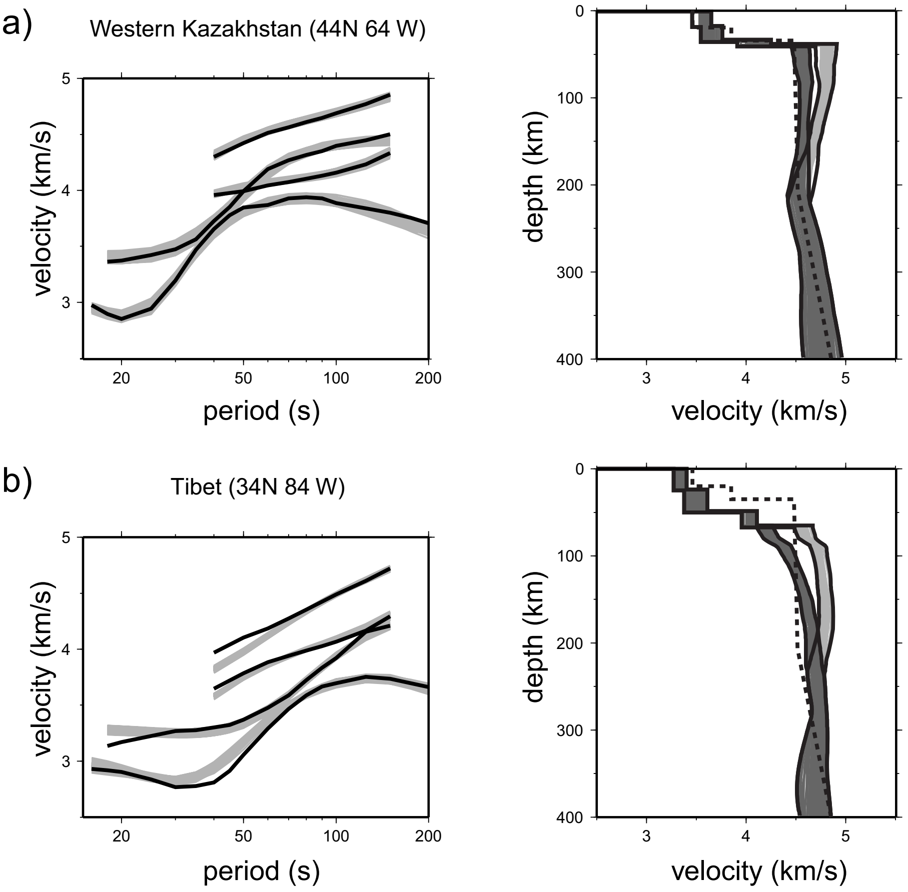

Figure 8: Results of the inversion for an ensemble of acceptable shear velocity models at two points: (a) Western Kazakhstan (44 N, 64 E) and (b) Tibet (34 N, 84 E). Left frames show four dispersion curves obtained from tomographic velocity maps (thick black lines) and the predictions from the ensemble of acceptable models (gray lines). Right frames show the ensemble of acceptable models. SV and SH velocities are shown with dark and light gray lines, respectively. The corridor of acceptable values is indicated with the solid black line. The global reference model AK135 (Kennett *et al.*, 1995) is plotted as the dashed line.

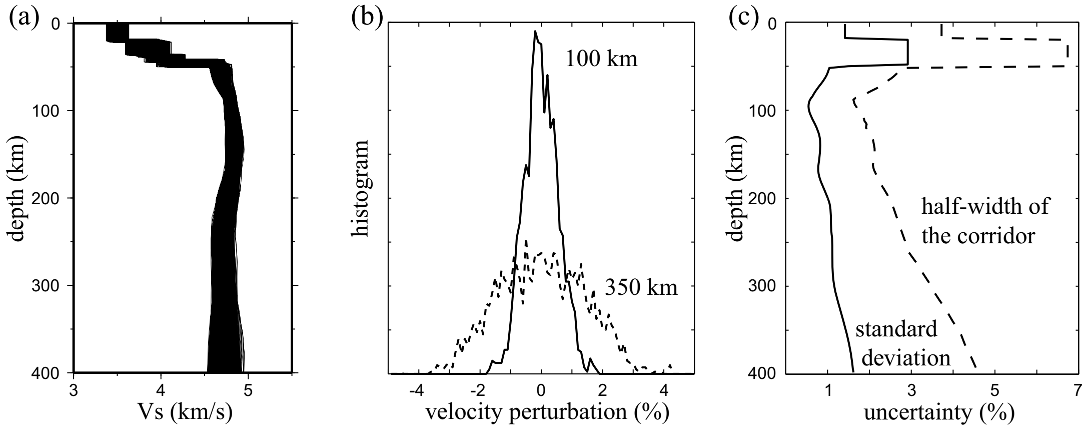

Figure 9: (a) Ensemble of acceptable 1D models obtained during the inversion of broadband surface-wave dispersion data at a point in the East European Platform (54N 30E). Only isotropic parts of the models are plotted. (b) Histograms of velocity perturbations at two depths: 100 km (solid line) and 350 km (dashed line). (c) Estimates of uncertainty obtained using the ensemble of acceptable models. Standard deviation of velocity at each depth is shown with the solid line. The half-width of the corridor of acceptable values is shown with the dashed line.

AK135 as the reference here. We say that the perturbation is "persistent" only if it appears in every member of the ensemble. In other words, the perturbation at a particular depth is persistent if its value is larger than the half-width of the corridor.

Statistical properties of an ensemble of acceptable models in a point in the East European Platform, full-width, etc.. (54^oN 30^oE) are shown in Figure 9. The velocity distribution at each depth is approximately Gaussian.

3. Overview of Results of Inversion

The inversion produces an ensemble of acceptable models at each spatial node on a 2° × 2° grid world-wide. We summarize the ensemble of models with the "Median Model", which is the center of the corridor defined by the ensemble, and the uncertainties, which are identified with the half-width of the corridor at each depth. The features of the model that are worthy of interpretation are those that appear in every member of the ensemble of acceptable models. We call these features "persistent". and the uncertainties while concentrating discussion on the mantle part of the model.

3.1 Isotropic structure

Global inversion

Horizontal slices of the Median Model at several depths are shown In Figure 10. The large-scale anomalies are well known from previous global tomographic studies e.g.,Woodhouse & Dziewonski (1984), Nataf *et al.* (1986), Montagner & Tanimoto (1991), Zhang & Tanimoto (1992, 1993), Masters *et al.* (1996), Ekström & Dziewonski (1998), Mégnin & Romanowicz (2000). High-velocities appear beneath all shields. Continental low-velocities appear in tectonically deformed regions such as the Red Sea rift and in back-arc regions in subduction zones. Age dependent lithospheric thickening and asthenospheric thinning is also evident beneath oceans.

A more detailed inspection of the model (e.g., Figure 11a) reveals smaller scale features that are not apparent in previous global tomographic models. Some of these features at high southern latitudes are discussed by Ritzwoller *et al.* (2001) and in Central Asia by Villaseñor *et al.* (2001).

This can also be seen clearly in Figure 12 where we present several vertical slices of isotropic upper mantle v_s. Figure 12b shows the average velocity perturbations for profile $A-A'$ crossing India, Tibet, Tarim Basin, Tian-Shan, Kazakhstan, and Southern Siberia. At depths less than 200 km, there is a high-velocity zone corresponding to thickened lithosphere that is especially well developed beneath India and Tibet. A strong low-velocity zone can be seen beneath India at depths larger than 200 km. The shallow low-velocity zone underlying northern Tibet is also apparent on the 80 km depth slice (Fig 11a). Figure 12c presents the uncertainties of the velocities along profile $A - A'$. Consistent with the world-wide average, the amplitude of the uncertainty increases from 1-3% at the top of the mantle to more than 6% at 400 km, but the amplitude of velocity anomalies decreases with depth. The solid black contour on the vertical slices (Figures 11b, d, e) encloses the persistent model features; i.e., those features with amplitudes larger than the uncertainty. Most of the model features below 250 km are not persistent.

Figure 12d and 12e show two other vertical slices, one across northern Eurasia and the other across the northern Pacific. The northern Eurasian profile crosses two major shields, the European platform and the Siberian shield, and shows high-velocity lithosphere beneath both shields. The thickness of the lithosphere varies along the profile and at some points appears to reach ~250 km. The structure below the lithosphere is not resolved. The northern Pacific slice reveals a number of persistent features, including: (1) a low velocity zone beneath western United States, (2) a high-velocity oceanic lithosphere with systematically increasing thickness with age underlain by a low-velocity asthenosphere, (3) a high-velocity anomaly corresponding to the lithosphere subducting beneath Japan resolved up to ~150 km depth, and (4) a back-arc low-velocity zone beneath the Sea of Japan. The structure below 250 km is unresolved in most of places.

We summarize by noting that the surface-wave data appears to produce persistent isotropic features at horizontal and vertical length scales that represent an improvement over previous global surface wave studies in many places. The data resolve isotropic S-wave

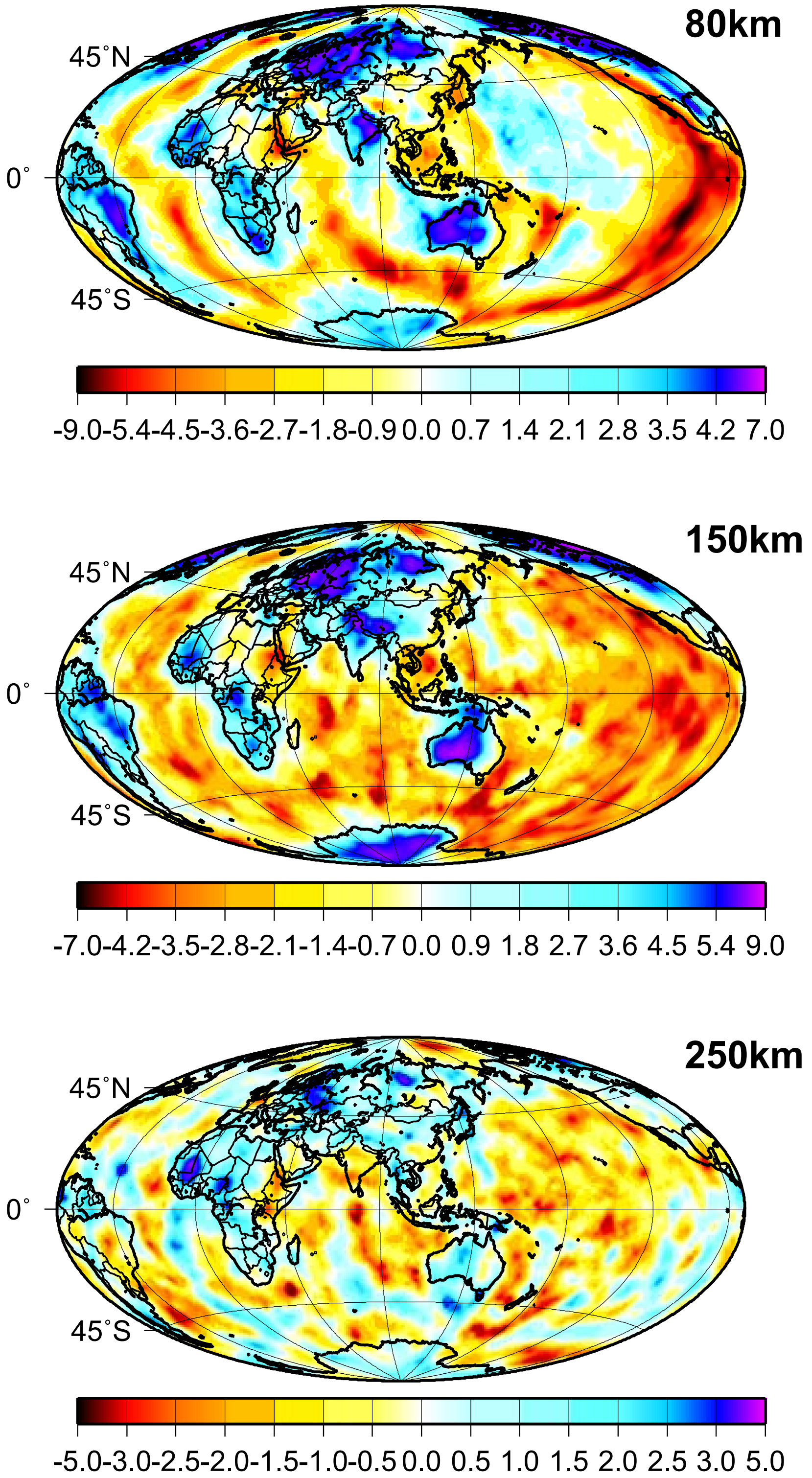

Figure 10: Perturbations of the average isotropic S-wave velocities at the uppermost mantle, and depths of 80, 150, and 250 km.

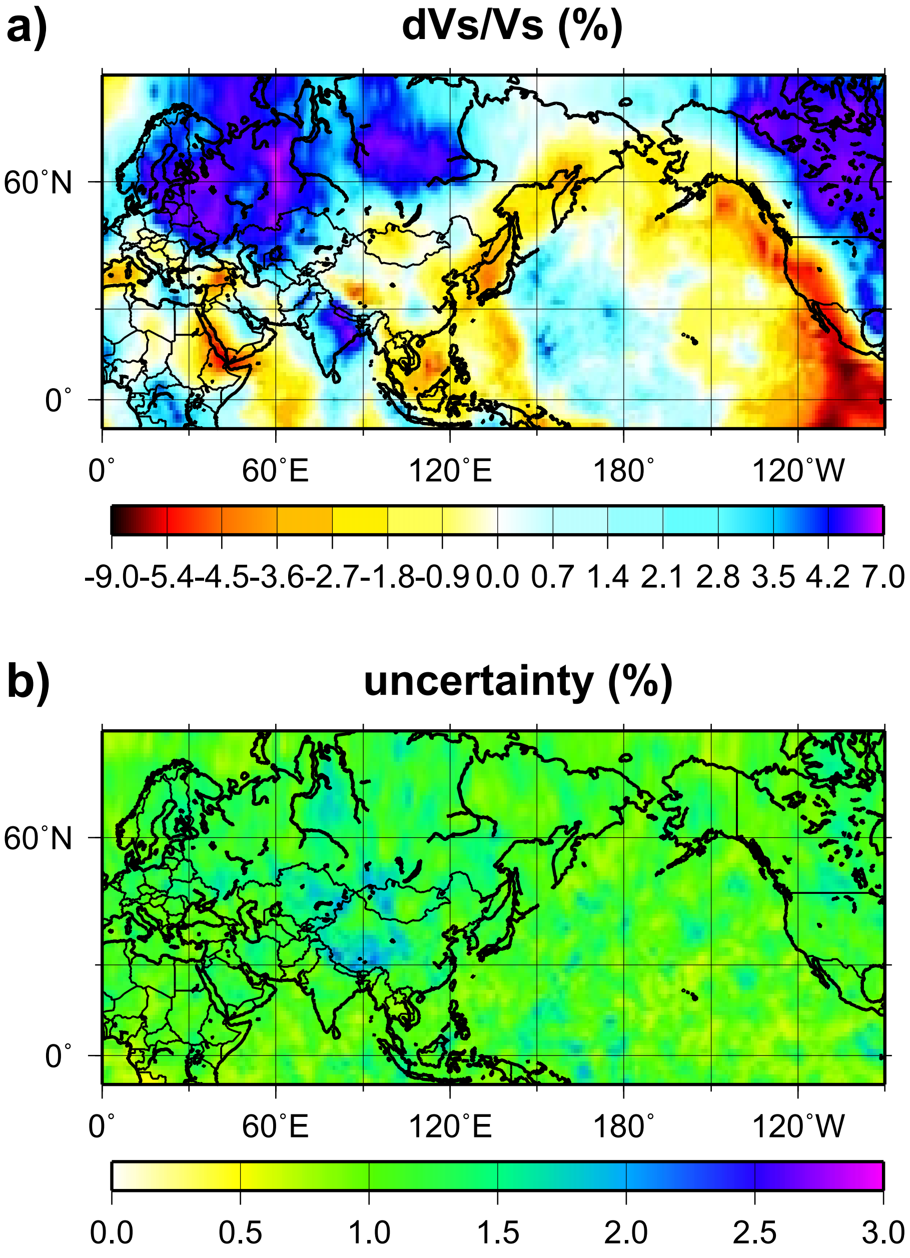

Figure 11: (a) Perturbations of the average isotropic S-wave velocity at 80 km beneath the Eurasian-Pacific region. (b) Uncertainty of the average velocity at 80 km defined as half-width of the corridor of acceptable values.

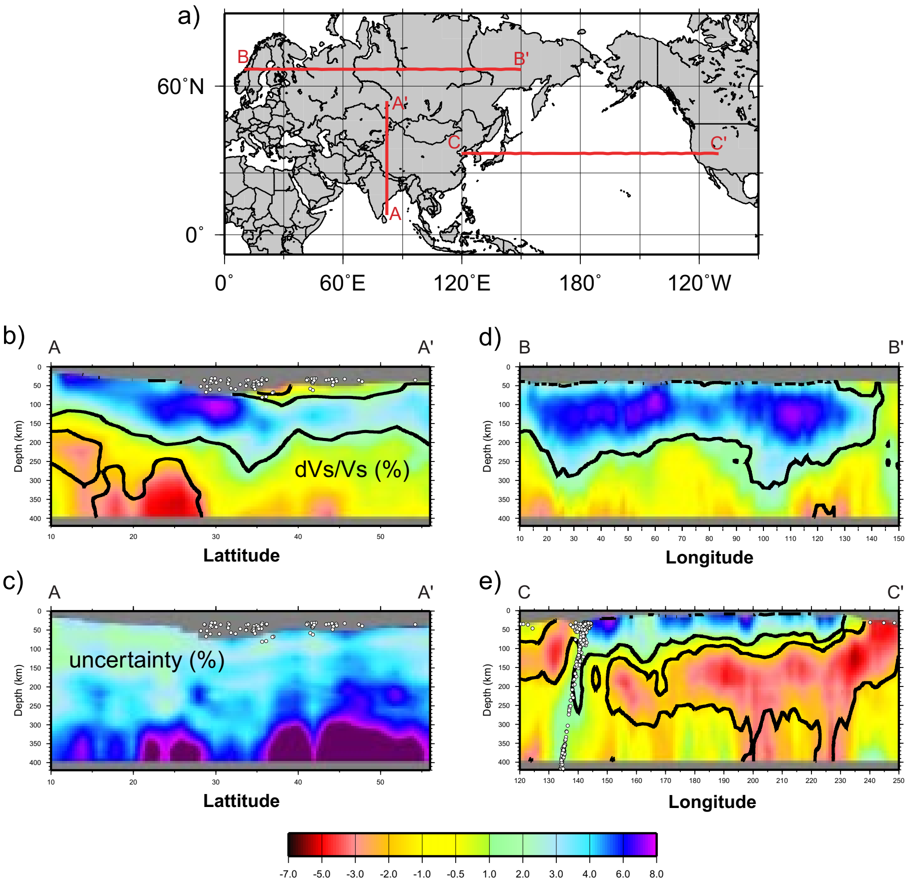

Figure 12: Vertical slices of the distribution of the average S-wave velocity. (a) Map showing locations of three profiles. (b), (d), and (e) Perturbations of the average S-wave velocity beneath the three profiles shown in frame (a). Black contours outline the persistent velocity anomalies. (c) Uncertainties of the average S-wave velocity for the profile A-A'. The same color scale is used for average values and uncertainties.

anomalies to depths of $\sim$ 250 km. At larger depths, only rare extremely strong anomalies are identified as persistent.

3.2 Radial anisotropy

As mentioned previously, over most of the earth long period Rayleigh and Love wave dispersion curves are 'inconsistent' in the sense that they cannot be fit simultaneously using a simple isotropic model. Similar to many previous studies e.g.,McEvilly (1964), Dziewonski & Anderson (1981), Gaherty & Jordan (1995), Montagner & Jobert (1988), Montagner & Tanimoto (1991), Ekström & Dziewonski (1998), Villaseñor *et al.* (2002) we resolve this Rayleigh-Love discrepancy by introducing radial anisotropy in the upper mantle. It is true that this discrepancy can be resolved either by introducing very low P-wave speeds in the crust (e.g., Figure 13) or by allowing fine-scale oscillations in S-wave speed in the uppermost mantle e.g., Mitchell (1984). We do not consider either alternative to be physically plausible, first, because they would have to be ubiquitous features of the upper mantle and, second, because independent evidence for anisotropy in the upper mantle is now overwhelming (e.g., from receiver function amplitudes versus azimuth and shear wave splitting).

In addition, while an oscillatory upper mantle can be successful in some locations, it cannot produce a satisfactory model everywhere. In particular, in tectonically deformed regions, the inversion with the isotropic parameterization produces a high-velocity subcrustal lid with an extremely high S_n velocity ($>$ 5 km/s) that is inconsistent with recent models of S_n velocities (Ritzwoller *et al.*, 2001). Radial anisotropy is able to resolve the Rayleigh-Love discrepancy because Rayleigh and the Love waves are sensitive to different S-wave velocities, v_{sv} and v_{sh} respectively, two of the five elastic moduli that compose a radially anisotropic model.

In Figure 14a we show the distribution of the strength of radial anisotropy in the Median Model, described by parameter ζ defined as:

$$\zeta = \frac{v_{sh} - v_{sv}}{v_{sv}}, \tag{9}$$

where v_{sv} and v_{sh} are taken at the top of the radially anisotropic upper mantle (Smith & Dahlen, 1973).

In most regions, $\zeta \sim 4\%$ which is similar to the value in PREM. Stronger anisotropy is found in some oceanic regions and in some tectonically deformed zones within continents (e.g. Tibet, Iran, eastern Africa). There are no significant anomalies with negative radial anisotropy ($v_{sv} > v_{sh}$). The local uncertainty in the strength of the anisotropy is shown in Figure 14b and averages about 2%. In most places radial anisotropy in the upper mantle is a persistent model feature, but in a few relatively small regions radial anisotropy cannot be resolved. However, while radial anisotropy is generally persistent, its uncertainty is relatively large, averaging about 50% of the observed value.

Radial anisotropy can only be resolved unambiguously by incorporating short and intermediate period measurements in our whole data-set.

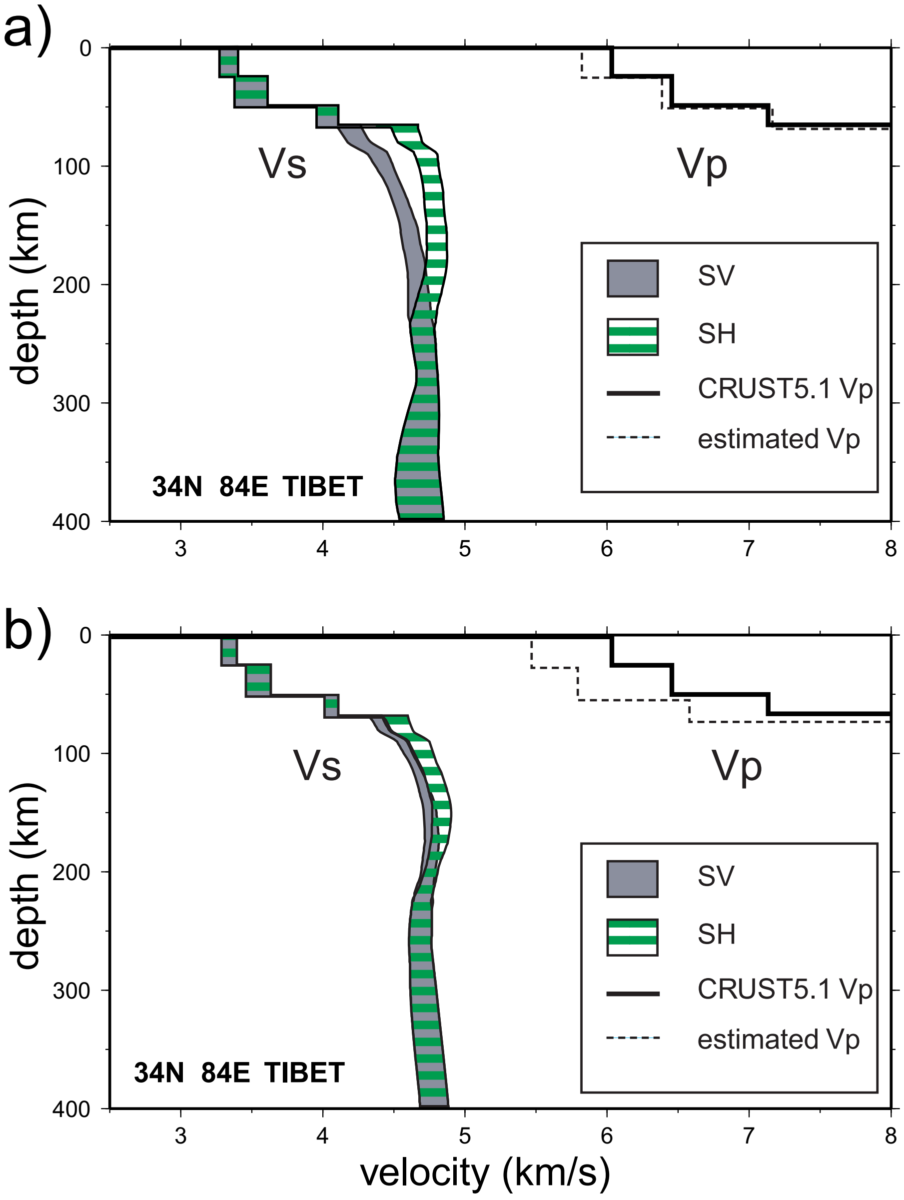

Figure 13: Examples of inversions at a point in Tibet illustrating the trade-off between the strength of radial anisotropy and the crustal P-wave speed. During the inversion shown in frame (a) the CRUST5.1 values of the crustal P-wave velocity have been used in the reference models. In case (b) these velocities have been reduced by 10%.

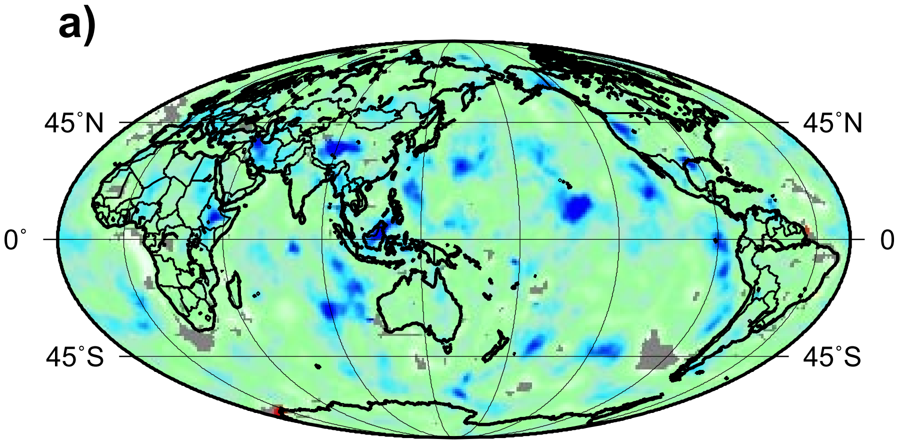

strength of the radial anisotropy (%)

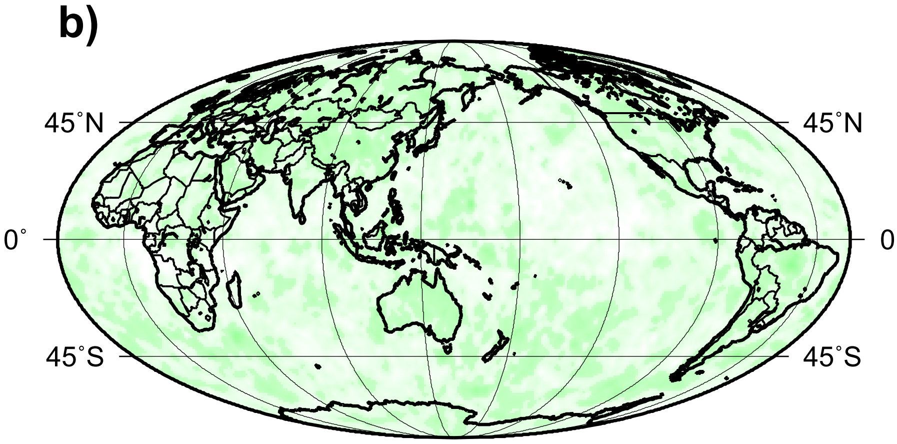

uncertainty of the anisotropy (%)

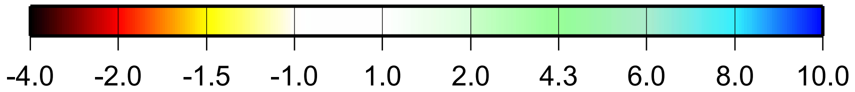

Figure 14: (a) Global distribution of the strength of radial anisotropy: $\zeta = \frac{\beta_h - \beta_v}{\beta_v}$. Regions where the anisotropy cannot be resolved are shown with gray. (b) Uncertainty in the strength of radial anisotropy. The same color scale is used for average values and uncertainties.

In summary, a simple PREM-like parameterization of radial anisotropy is sufficient to fit Rayleigh- and Love-wave dispersion measurements world-wide and resolve the Rayleigh-Love discrepancy. Even using this simple parameterization, we obtain very large ($\sim 50\%$) uncertainties in the strength of radial anisotropy. Increasing the number of parameters describing the radial anisotropy would increase uncertainties further and reduce the resolution. Therefore, we conclude that more complicated vertical patterns of radial anisotropy cannot be resolved using surface-wave data alone.

3.3 Barents Sea inversion

This inversion is done at each node of a 1° × 1° grid across the region of the study

The inversion results are presented as deviations in shear-wave speed (in percent) from the S-wave speed in the 1-D *Barey* model. Figure 10 shows several horizontal slices through the model in the range from 60 to 280 km depth. The horizontal slice for a depth of 40 km is shown in Figure 11 together with the 1-D reference model *Barey.* The shear velocity cross-sections along several transects across the studied region are shown in Figure 12. The position of these transects are plotted on the map in Fig. 11. The 3-D model BARMOD reveals lateral heterogeneities in shear-wave speeds in the upper mantle across the whole region. Of particular interest are the imprints of first-order changes in the tectonic regimes, such as the mid-Atlantic ridge, the continent-ocean transition in the Norwegian Sea, and the thickened crust beneath Novaya Zemlya.

The structure of the lithosphere is naturally very closely related to its tectonic history. For the Barents Sea region, the evolution is characterized by repeated cycles of compression and extension. In a simplified view, we can reduce the evolution of currently observable structures to three main stages, all with a near west-east direction: (1) compression in early Paleozoic times related to the orogenesis of the Caledonides, (2) the Caledonian collapse accompanied by extension in the mid Paleozoic, and (3) compression in the late Paleozoic related to Uralian collision (Gudlaugsson *et al.* 1998 and references therein). We believe that the high-velocity anomaly dipping eastward beneath Novaya Zemlya (Fig. 12) is most likely not of thermal but of compositional origin and may be related to Caledonian and/or Uralian collision. The thickening of the anomaly beneath the Eastern Barents Sea basin, which evolved during late Permian – early Triassic times by rapid, non fault-related subsidence (Gudlaugsson *et al.* 1998), indicates a possible chronological relation of both processes (thickening in the mantle and subsidence in the crust), which in turn correlates in time with the Uralian collision. The location of the Caledonian suture in the Barents Sea region remains the subject of scientific debates, but Breivik *et al.* (2002) showed evidence that it may be situated in the western Barents Sea, approximately at the western boundary of the shallow upper mantle high-velocity anomaly. Thus, this western boundary is likely to be related to lithosphere subducted during the Caledonian collision. For the Uralian collision, no clear onset of a subducting slab as an indicator for a suture location can be identified in the model

To the west, BARMOD nicely images the imprints of the mid-Atlantic ridge and the

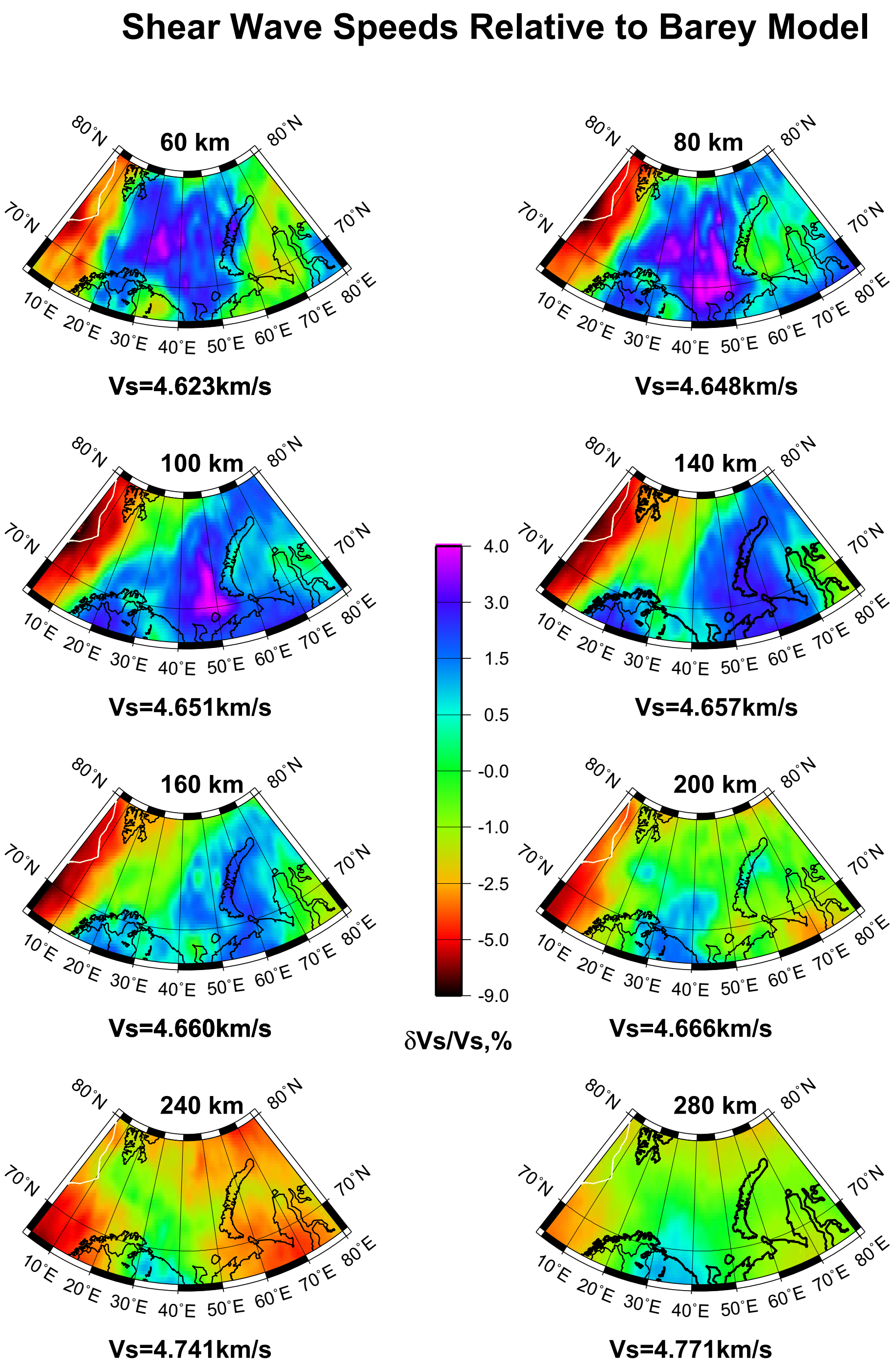

Figure 15: Results of the 3-D tomographic inversion: isotropic shear wave velocities $V_s = (V_{sv} + V_{sh})/2$ at different depths relative to the 1-D model. The reference S velocities are presented below each map.

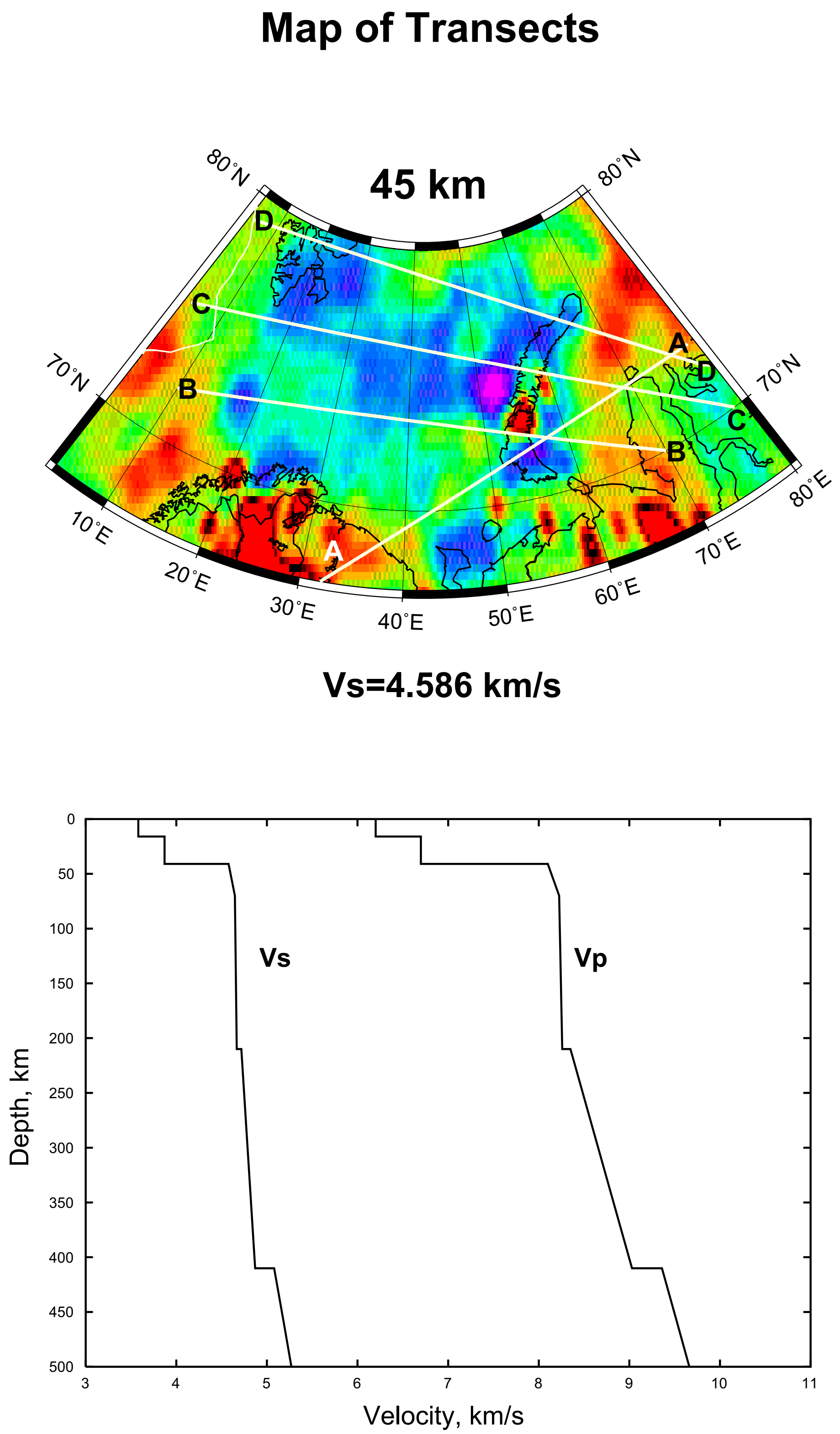

Figure 16: Results of the 3-D tomographic inversion: isotropic shear wave velocities $V_s = (V_{sv} + V_{sh})/2$ at 45 km relative to the 1-D model (top). The map contains in addition the position of the different transects through the model as shown in Fig. 13. The model *Barey (Schweitzer & Kennett 2002) used in this study as 1-D reference model is shown at the bottom.*

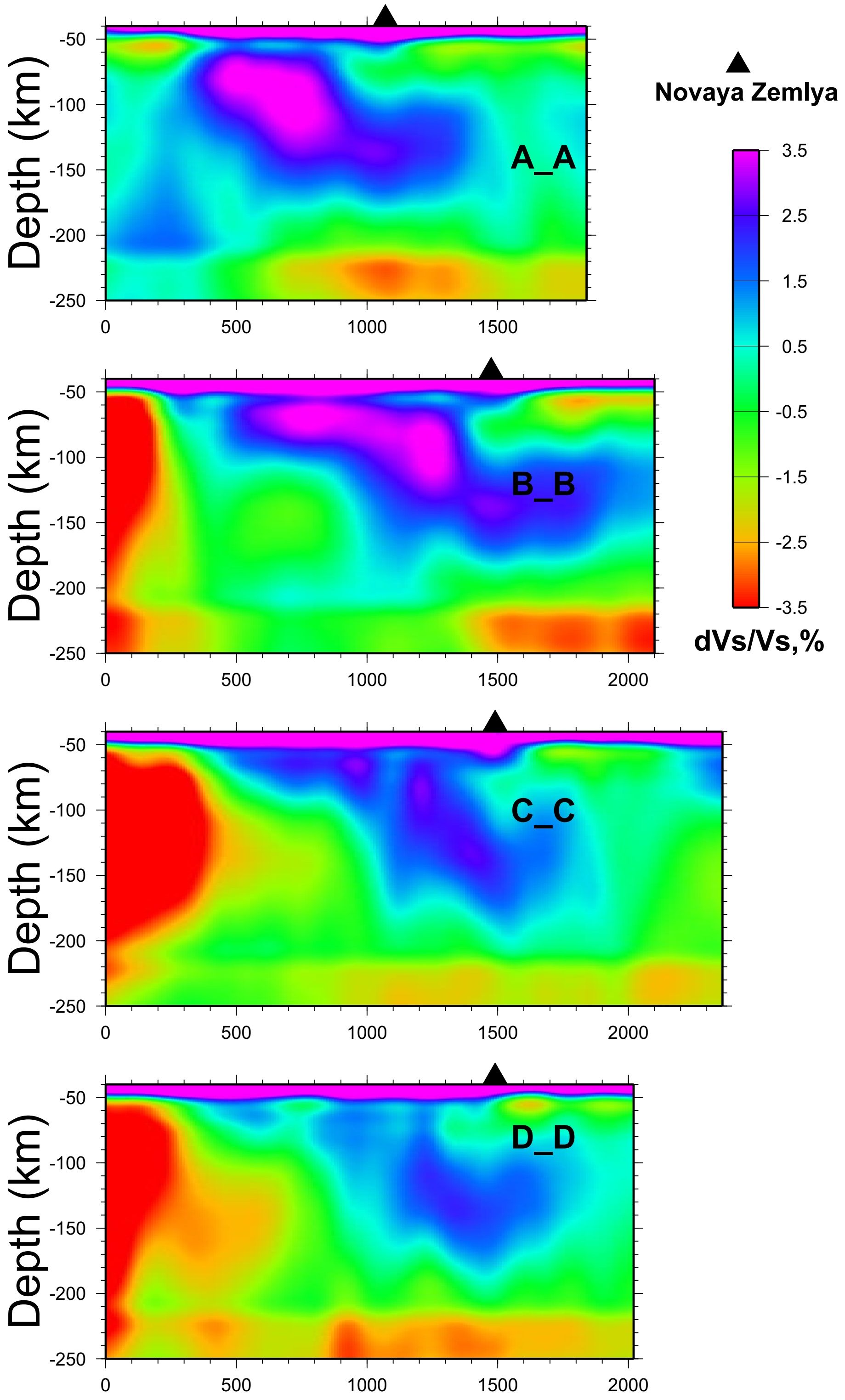

Figure 17: Isotropic S-velocity ($V_s = (V_{sv} + V_{sh})/2$) perturbations r elative to the *Barey* model along four transects shown in Fig.12.

extension of a low-velocity anomaly beneath the continental lithosphere near the Svalbard Archipelago. In contrast to the high-velocity anomaly to the east, this low velocity anomaly probably is thermal in origin, related to break-up of the north-eastern Mid-Atlantic during the Cenozoic. Faleide *et al.* (2006) compared BARMOD with thermal modeling across the Continent-Ocean-Boundary (Breivik *et al.* 1999) revealing a clear correlation between the modeled isotherms and the velocity field.

The velocity variations at 40 km depth, presented in Figure 11, reveal approximately the lateral change in S-wave velocity relevant for Sn propagation. Engdahl & Schweitzer (2004a; 2004b) described pronounced differences in travel times and waveform shapes on NORSAR array recordings of nuclear explosions conducted both at the northern and at the southern nuclear test side on Novaya Zemlya. This observation may be explained by multipathing effects due to the dipping high velocity body.

4. Higher mode tomography

There are some regions at the continents where relatively shallow earthquakes generate well observable crustal higher modes. In our experience, one of such regions is Central and South-East Asia where we were able to obtaine a significant amount of observations of the 1st overtone of Rayleigh and Love waves in the period range 7-15s. The resulting tomographic maps are shown in Figure 18. Joint Inversion of these data with data from fundamental mmodes helps to improve the vertical resolution in the crust (see Figure 19).

5. Rayleigh Wave Attenuation tomography

The knowledge of vertical and lateral variations of attenuation parameters in the Earth's crust and upper mantle is essential for understanding the tectonic setting of different regions. Professor Mitchell will describe such work based on his studies of Lg wave and its coda, as well as short-period surface waves. The attenuation model for Rayleigh surface wave may help to calibrate the determination of surface wave magnitudes on a regional base and by this way to extend the teleseismic Ms-mb event discriminant to regional distances. This will improve monitoring facilities of system for detection of weak nuclear explosions. I will briefly describe very recent results in building the model for attenuation of Rayleigh waves in Central Asia. This model is defined by maps of attenuation across the region of study in the specifed period band (12-22 s). The first stage in model construction is the measurement of Rayleigh wave spectral amplitudes. Inherent difficulties result from multipathing and scattering of short-period surface waves crossing strong lateral inhomogeneities in the crust. These difficulties may be overcome by using FTAN or a special software SWAMTOOL designed at Las Alamos National Lab (USA), which incorporates dispersion analysis, phase-matched filtering, and additional means to estimate the quality and reliability of the measurements.

At the second stage of the work, spectral attenuation coefficients are estimated using both inter-station measurements and single station measurements corrected for the source and receiver terms.Corrections are done using the global 3D model CUB2 (Shapiro & Ritzwoller, 2002).

The third stage of this work is tomographic inversion of the measurements for the attenuation model; maps of attenuation for the region and frequency band of study.

Examples of obtained maps of the attenuation coefficient γ_R and factor Q_R for a set of periods are shown in Figures 20 and 21.

6. Application of a global 3D model to improve regional event locations

Accurate location of weak seismic events is crucial for monitoring clandestine nuclear tests, for studying local seismic structures, and for assessing possible seismic hazards. Outside of a few regions with dense seismic networks, weak seismic events (with magnitude less than 4) are usually sparsely recorded at epicentral distances less than 20^o. Because of lateral variations in crustal and upper mantle structures, observed travel times of seismic phases deviate significantly from predictions based on 1-dimensional (1D) seismic models. Accurately locating weak seismic events remains a difficult task for modern seismology. Perhaps the most promising solution to this problem is the use of a 3-dimensional (3D) model of the Earth.

Conversion of 3D S velocity model to 3D P velocity model

As P waves play dominant role in any location technique it is necessary to convert the obtained S velocity model of the mantle into P velocity model. There are two general approaches to doing this. The first is to use "empirical scaling relations" that convert S-wave anomalies into P-wave anomalies. The most successful of these, map shear-speed perturbations, δv_s, relative to a reference S-model, v_{s_0}, to compressional-velocity perturbations, δv_p, relative to a reference P-model, v_{p_0}, where $d \ln v_p / d \ln v_s$ is then taken to be an empirically constrained constant that may be a function of depth, but is usually depth invariant. The second approach is to use a "theoretical conversion" based on laboratory measurements of thermoelastic properties of mantle minerals and on models of the average mineralogical composition of the mantle. We convert only isotropic v_s to v_p. In the radially anisotropic part of CUB2.0 we, therefore, use $(v_{sv} + v_{sh})/2$.

We prefer the theoretical conversion from v_s to v_p for two reasons. First, as we will show below, the theoretical conversion appears to work somewhat better in that the regional P and P_n empirical phase path anomalies are fit better by travel times predicted by empirical model. Second, the theoretical conversion leads naturally to future improvement. It can be regionally tuned in a physically meaningful way by modifying the mineralogical composition and temperatures within the anelastic model, and it can be updated as better mineralogical data become available.

Figure 22a shows the resulting v_s to v_p theoretical conversion. Figure 22b displays this conversion presented as the logarithmic scaling relation, $d \ln v_s / d \ln v_p$, which varies with both v_s and depth. The v_s profile from AK135 is overplotted, nearly paralleling the contours of the theoretical predictions. This illustrates why depth-independent values of the scaling relation tend to work fairly well in the upper mantle. For the values of v_s in AK135, the theoretical prediction for the scaling relation is $d \ln v_s / d \ln v_p \sim 1.6 - 1.8$. Figure 22b also shows that the v_s profile converted from the AK135 v_p profile by the theoretical conversion agrees fairly well with the v_s profile in AK135 at depths below about 100 km. The theoretical conversion between v_s and v_p differs appreciably from the v_s and v_p p arts of AK135 above about 100 km. Thus, in the shallower parts of the mantle, v_p computed using the theoretical conversion will differ appreciably from v_p computed using the logarithmic scaling relation applied to reference values from the 1-D model AK135.

Location experiment

Here we present the results of a validation test in which, using the described above 3D model of the crust and upper mantle and regional phase data alone, we relocate ~ 340 earthquakes and nuclear explosions in Eurasia. The event locations using the 3D model are compared with so-called Ground Truth (GT) data, either known by non-seismic means or validated by cluster analysis, with location accuracy mostly 5 km or better. To locate seismic events using only regional Pn and P phases we apply the grid-search technique. A grid 50 × 50 km with 1 km spacing is built around a reference point known from teleseismic information taken from PDE or EHB (Engdahl *et al.*,1998) catalogs. For each point of the grid and each observed arrival we calculate travel times of Pn and P waves as predicted by our model. Travel times for each phase are found using so-called Source Specific Correction Surfaces (SSSCs) which were calculated beforehand for more than 800 seismic stations. Each SSSC is a multi-level table of travel times for Pn and P waves propagating in our 3D model, each level corresponds to a certain source depth and contains travel times on a grid of azimuthal directions from the station to epicentral distances less than 20^o. Actually, there are not full travel times but corrections relative to 1D-model (typically, AK135). These corrections are found by 2D ray tracing through the 3D model using technique developed by Červený & Pšenčík (1984). An example of SSSC is shown in Figure 23.

We estimate rms-misfit of predicted and observed travel times for all observed phases in each point of the grid and select the node with minimal rms as a new location (Figure 24). Location errors for 3D and 1D location for explosions on Lop Nor test site in China and earthquakes in Racha seismic zone, Georgia, relative to ground truth locations is shown in Figure 25. One can see strong bias in locations with 1D model.

The statics of relocation for a set of 16 clusters shows significantly better accuracy achieved using 3D location (Tables 1 and 2). Results of random selection experiment in which we use for relocation different combinations of n stations for different values of n show that 3D location produces more accurate results than 1D location in 70-75% of all cases (for

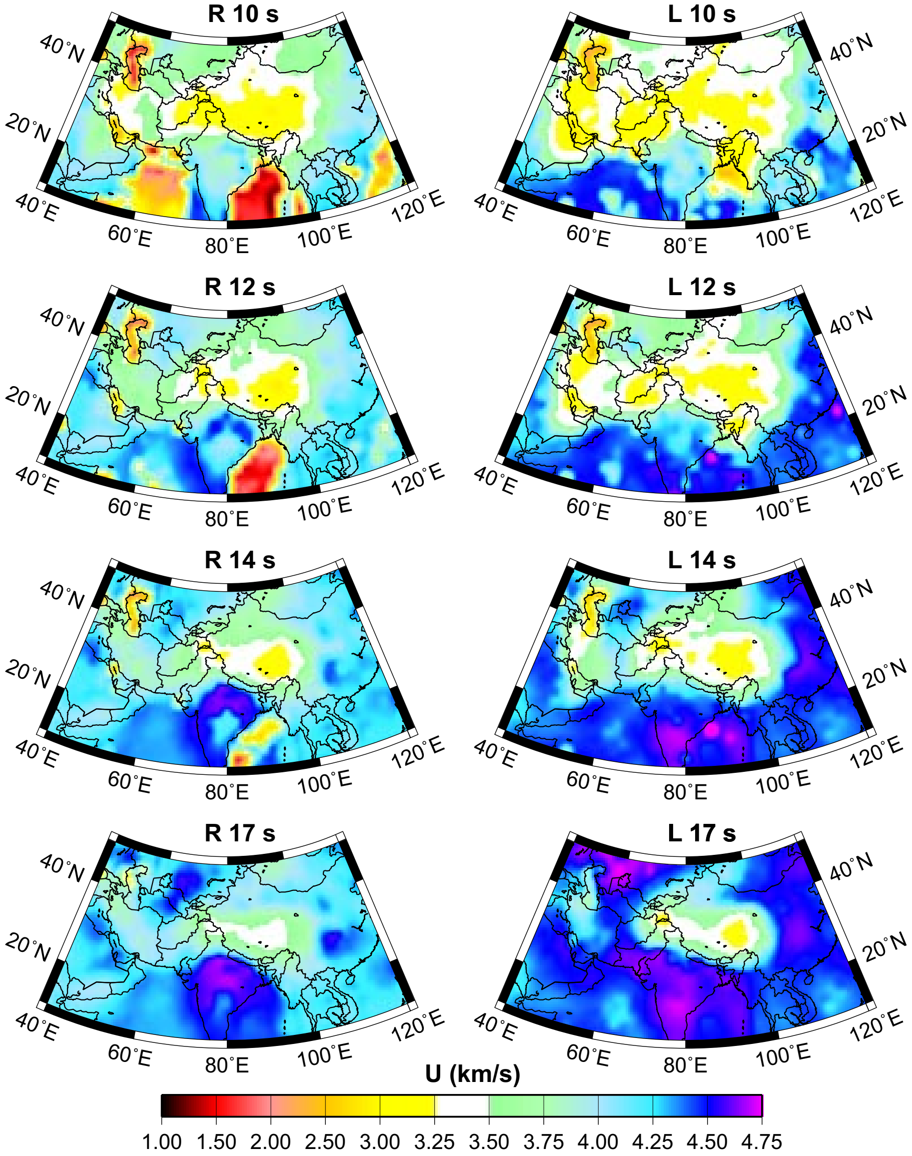

Figure 18: Group velocity maps for the first higher modes at the indicated periods: (left) Rayleigh mode and (right) Love mode.

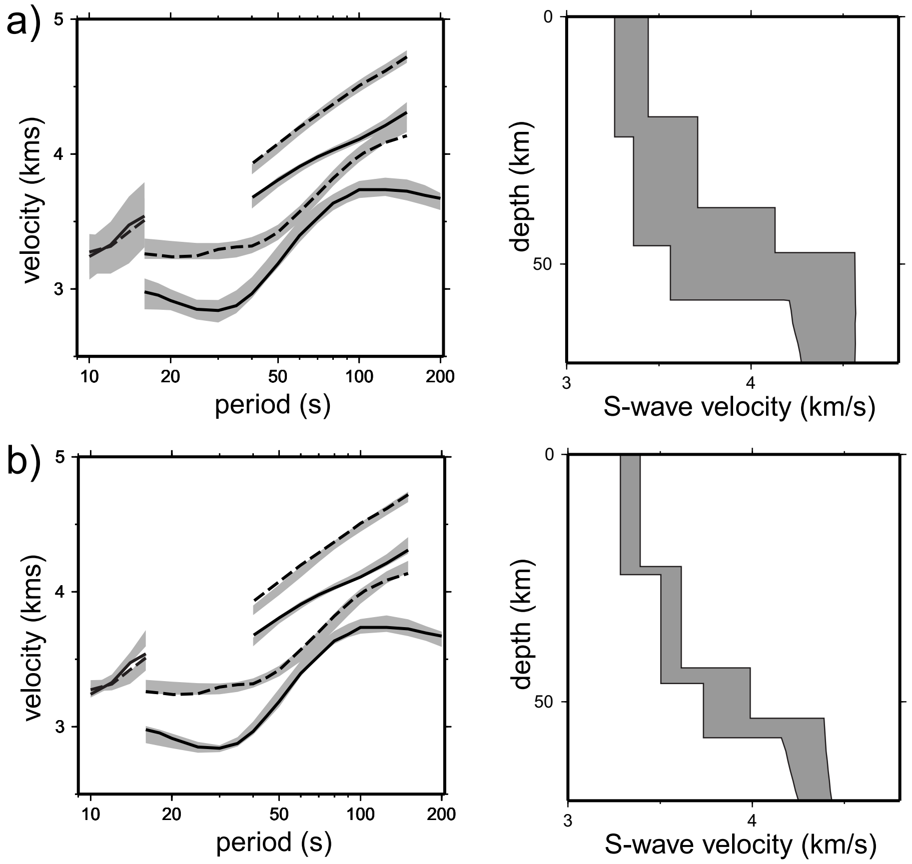

Figure 19: The example of the Monte-Carlo inversion of observed data for a shear velocity profile for a location in South-Western China (30°N, 100°E). Left panels display the observed curves as solid (Rayleigh) and dashed (Love) black lines. Rayleigh and Love wave fundamental mode group (U_0) and phase (C_0) velocities are shown together with Rayleigh and Love wave first higher-mode group velocities (U_1). Gray dispersion curves are computed from the range of models shown in the right panel. Right panels display the range of models that fit the data. (a, Top Row) Only fundamental mode data are used in the inversion. (b, Bottom Row) Both fundamental and overtone data are jointly used in the inversion. The joint inversion reduces the range of acceptable models in both the crust and the mantle and reduces the range of crustal thicknesses while fitting all data acceptably.

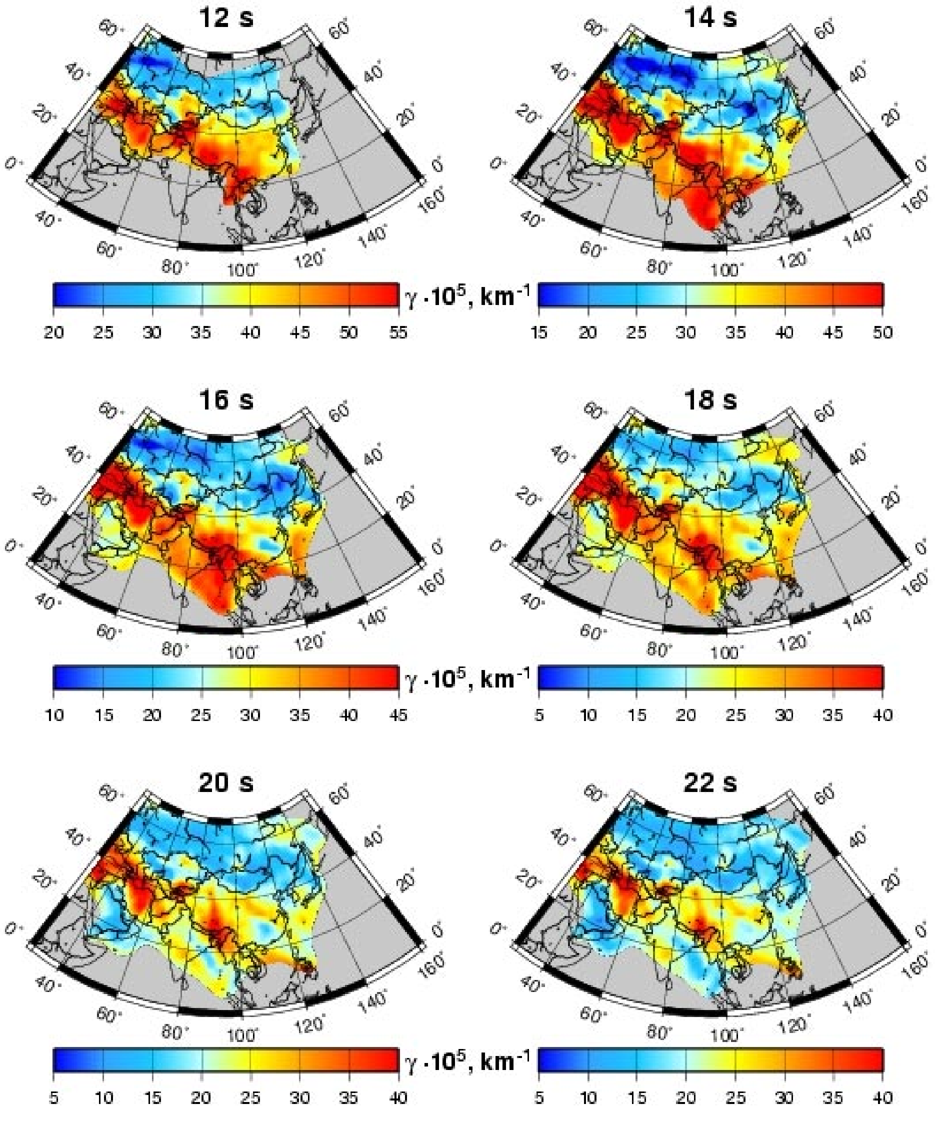

12 s

14 s

16 s

18 s

20 s

22 s

Figure 20: Maps of Rayleigh wave attenuation coefficients at the indicated periods.

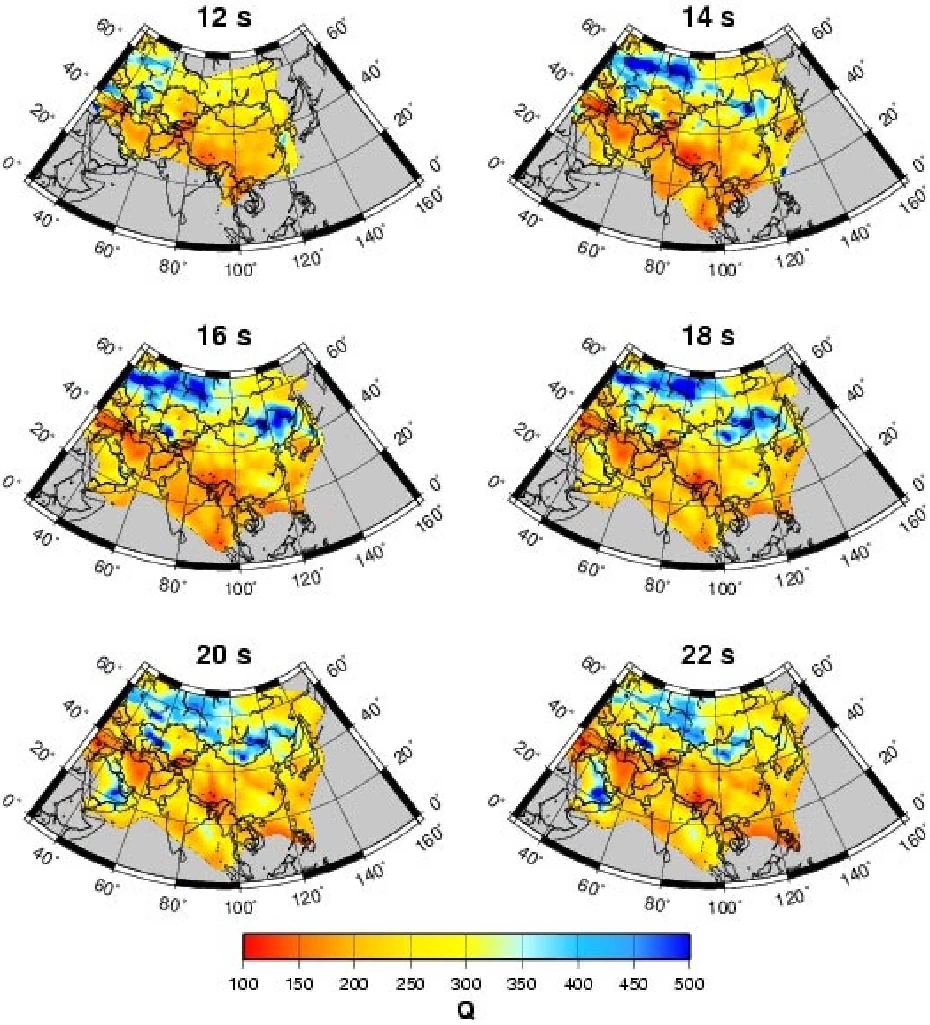

Figure 21: Maps of Rayleigh wave Q_R factor at the indicated periods.

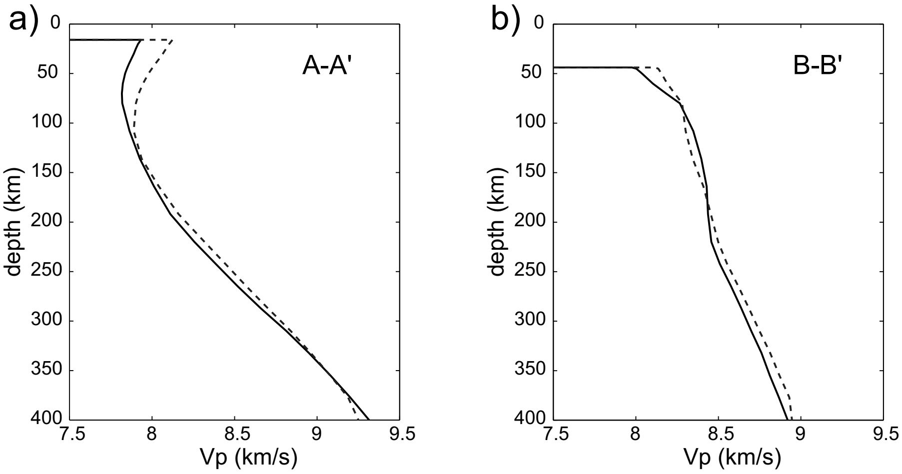

Figure 22: v_p model at the mid-points of profiles (a) $A-A'$ and (b) $B-B'$ from Figure 12. The solid line represents the theoretical conversion from v_s and the dashed line is from the empirical scaling relation $d\ln v_s/d\ln v_p = 2.0$ in which AK135 is used as the reference.

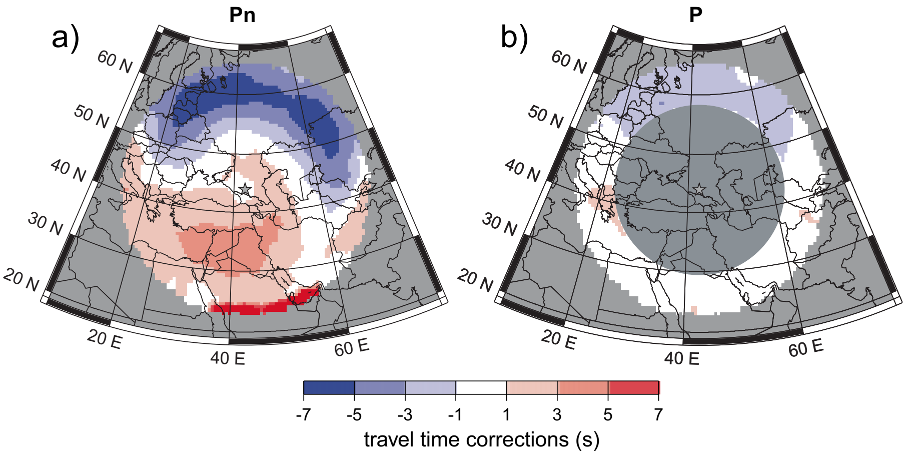

Figure 23: Example of P_n and P travel time correction surfaces computed for a surface source for station KIV. The corrections here are relative to the 1-D model AK135

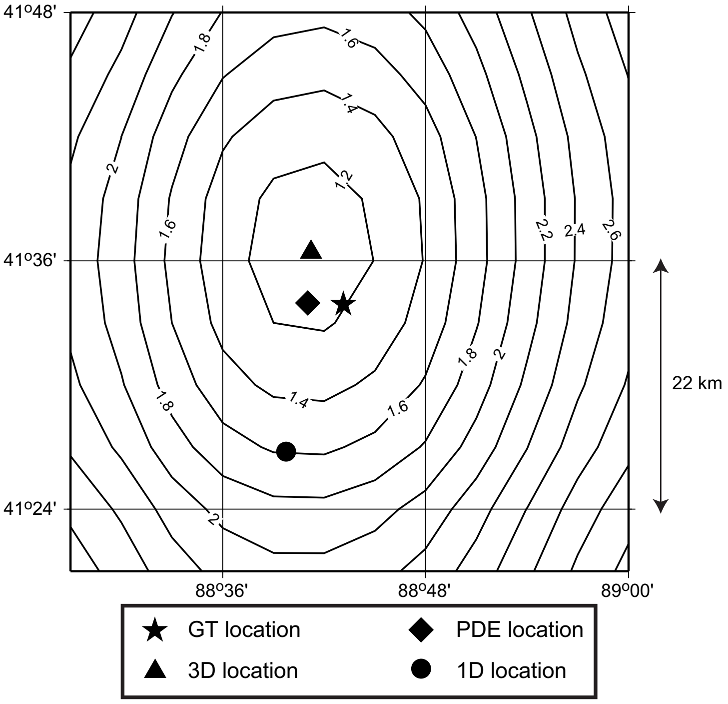

Figure 24: Contours of rms-misfit using the 3-D model CUB2.0_TH for a grid of hypothesized epicenters for an explosion at the Lop Nor test site (May 26, 1990; 54 reporting stations). Units are seconds. The GT1-2 location is indicated with a star, the best-fit locations using the 3-D and 1-D models are shown with a triangle and a circle, respectively, and the PDE location is shown with a diamond.

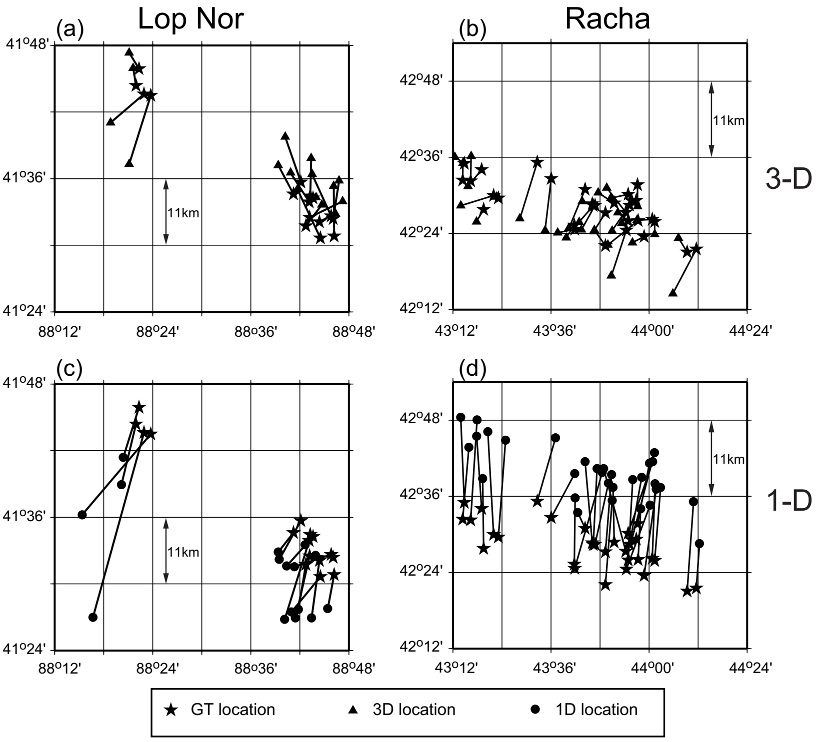

Figure 25: Mislocation vectors from two event clusters for (left column) explosions on the Lop Nor test site and (right column) earthquakes near Racha, Georgia. (a) and (b) 3-D model (CUB2.0_TH) locations. (c) and (d) 1-D model (AK135) locations. Stars mark GT locations, triangles and circles are 3-D and 1-D model locations, respectively

explosions and GT5 earthquakes), if $n \geq 5$. This test indicates that the location of regional events can be significantly improved by using a global 3D model. More details are presented in Levshin & Ritzwoller (2002), Ritzwoller *et al.* (2002b).

Table 1. Location results for nuclear explosions.

				CUB2.0_TH		AK135	
Cluster No.	Name	Events[a]	Stations[b]	Error[c]	RMS[d]	Error[c]	RMS[d]
1	Azgir	6	19	4.2	1.08	24.0	1.49
2	Balapan	10	25	3.9	1.10	11.2	1.22
3	Degelen	3	18	3.1	1.01	12.0	1.36
4	Lop Nor	16	45	6.1	1.22	9.6	1.49
5	Novaya	3	15	8.0	1.03	13.6	1.57
	overall[e]	38	24	5.1	1.09	14.1	1.43

[a] Number of events with open azimuth $< 180°$ and ≥ 5 stations.
[b] Median number of stations.
[c] Average distance from estimated to GT location, in km.
[d] Rms difference between observed and predicted travel times, in sec.
[e] Total or average of cluster values.

Table 2. Location results for GT5 earthquakes.
Terminology similar to Table 1.

				CUB2.0_TH		AK135	
Cluster No.	Name	Events	Stations	Error	RMS	Error	RMS
7	Adana	19	23	8.8	1.04	8.1	1.17
8	Bhuj	4	15	11.5	1.00	8.5	1.42
9	Chamoli	50	17	10.8	1.20	20.8	1.54
10	Duzce	21	45	7.3	1.23	6.6	1.33
11	Erzin	8	33	6.0	1.29	9.5	1.61
12	Garm	26	21	5.2	1.12	9.7	2.17
13	Hoceima	21	26	4.4	0.90	7.5	0.86
14	Izmit	8	116	5.1	1.07	5.3	1.10
15	Koyna	8	10	5.5	1.13	10.7	1.23
16	Racha	34	20	8.2	1.15	21.8	1.43
17	Siberia	8	33	6.3	1.13	11.0	1.31
	overall	207	32	7.2	1.12	10.9	1.38

7. Conclusions

Two main characteristics of our global model of the crust and upper mantle distinguish it from previous global tomographic models. First, both vertical and lateral resolution are improved as a result of inverting a new broad-band data set of group and phase velocities and the use a-priori information to restrict the range of physically plausible models. A novel characteristic of the data set is the use o f a large number of group velocity measurements for both Rayleigh and Love waves.

The group velocity data contain short and intermediate period information that allows us to significantly improve the vertical resolution. A-priori information is required because surface wave data alone are insufficient to resolve all of the model parameters unambiguously. Therefore, we constrain crustal structures in order to help resolve the trade-off between crustal and upper mantle velocities and have identified and attempt to resolve other important trade-offs, such as that between the strength of radial anisotropy in the upper mantle and crustal P-wave velocities.

The second important characteristic of the model is that it contains estimates of uncertainties. The model, therefore, is perhaps the first global model with meaningful "error bars". The uncertainty estimates derive from a multi-step inversion procedure that culminates in a Monte-Carlo sampling of model space to produce an ensemble of acceptable models. The features that appear in every member of this ensemble are termed "persistent" and only these features are deemed to be worthy of interpretation. The uncertainty analysis indicates that our surface wave data resolve upper mantle structures to depths of about 250-300 km.

The procedure we describe here and the data set to which it is applied, open new possibilities for the study of the crust and upper mantle structure. Because of its relatively high lateral resolution, the model reveals anomalies at scales that are relevant to regional tectonics. The breadth of the frequency band improves vertical resolution which also important for interpretation. The uncertainty analysis allows us to select only those features of the model that most worthy to be interpreted in the framework of regional tectonic and geodynamical processes. The tests demonstrate applicability of the obtained model for improving location of weak events using regional data.

References

Barmin, M.P., Levshin, A.L., & Ritzwoller, M.H., 2001. A fast an reliable method for surface wave tomography, *Pure and Appl. Geoph.*, **158**, n.8, 1351-1375.

Barmin, M.P., Levshin, A.L. & Ritzwoller, M.H., 2005. Finite-frequency group velocity kernels for surface wave tomography, *EOS, Trans. Am. geophys. Un.* , **86(52)**, Fall Meet. Suppl., Abstract S51E-1057.

Bassin, C., Laske, G., Masters, G., 2000, The current limits of resolution for surface wave tomography in North America, *Eos Trans. AGU*, 81(48), F879, Abstract S12A-03.

Breivik, A.J., Verhoef, J., Faleide, J. I., 1999, Effect of thermal contrasts on gravity modeling at passive margins: Results from the western Barents Sea, *J. Geophys. Res.*, 104, 15293-15311.

Breivik, A.J., Mjelde, R., Grogan, P., Shimamura, H., Murai, Y., Nishimura, Y., Kuwano, A., 2002, A possible Caledonide arm through the Barents Sea imaged by OBS data, *Tectonophysics*, 355, 67-97.

Bungum, H., Ritzmann, O., Maercklin, N., Faleide, J.I., Mooney, W.D.& Detweiler, S.T., 2005, Three-dimensional model for the crust and upper mantle in the Barents Sea region, *Eos Trans. AGU*, 86, 160-161.

Červený, V., and I. Pšenčík, SEIS83 – Numerical modeling of seismic wave fields in 2-D laterally varying layered structures by the ray method, *Documentation of earthquake algorithms, Report SE-35*, E.R. Engdahl (ed.), pp. 36-40, Boulder: World Data Center A for Solid Earth Geophysics, 1984.

Dahlen, F.A. & Tromp, J., 1998. *Theoretical Global Seismology*, Princeton University Press, Princeton, New Jersey.

Dahlen, F.A. and Y. Zhou, 2006. Surface-wave group-delay and attenuation kernels, *Geophys. J. Int.*, **65**, 545-554.

Dziewonski, A.M. & Anderson, D.L., 1981. Preliminary reference Earth model, *Phys. Earth. Planet. Inter.*, **25**, 297-356.

Ekström, G. & Dziewonski, A.M., 1998. The unique anisotropy of the Pacific upper mantle, *Nature*, **394**, 168-172.

Ekström, G., Tromp, J., & Larson, E.W.F., 1997, Measurements and global models of surface waves propagation, *J. Geophys. Res.*, **102**, 8137-8157.

Engdahl, E. R., R. van der Hilst, and R. Buland, 1998. Global teleseismic earthquake relocation with improved travel time and procedures for depth determination, *Bull. Seismol. Soc. Am.*, **88**, 722 - 743.

Gaherty, J.B. & Jordan, T.H., 1995. Lehmann discontinuity as the base of an anisotropic layer beneath continents, *Science*, **268**, 1468-1471.

Kennett, B.L.N., Engdahl, E.R., & Buland, R., 1995. Constraints on seismic velocities in the Earth from travel times, *Geophys. J. Intl'*, **122**, 403-416.

Laske, G. & Masters, G., 1997. A global digital map of sediments thickness (abstract), *EOS Trans. AGU*, **78**, F483.

Levshin, A.L., Yanovskaya, T.B., Lander, A.V., Bukchin, B.G., Barmin, M.P., Ratnikova, L.I., & Its, E.N., 1989. Recording, identification, and measurement of surface wave parameters. In: *Seismic surface waves in a laterally inhomogeneous Earth* (Keilis-Borok, V.I., editor). Kluwer Academic Publisher, Dordrecht, 131-182.

Levshin, A.L., Ritzwoller, M.H., Barmin, M.P., & Villaseñor, A., 2001. New constraints on the Arctic crust and uppermost mantle: Surface wave group velocities, P_n, and S_n, *Phys. Earth. Planet. Inter.*, **123**, 185-204.

Levshin, A.L., and M.H. Ritzwoller, 2002. Application of a global-scale 3D Model to improve regional locations, Studia Geoph. et Geod., **46**, 2, 289-292.

Levshin, A.L., M.P. Barmin, M.H. Ritzwoller, and J. Trampert, 2005a. Minor-arc and major-arc global surface wave diffraction tomography, *Phys. Earth Planet. Ints.*, **149**, 205-223.

Levshin, A.L., M.H. Ritzwoller, and N.M. Shapiro, 2005b. The use of crustal higher modes to constrain crustal structure across Central Asia, **Geophys. J. Int.**, **160**, 961-972, 2005

Levshin, A.L., and G.F. Panza. Caveats in modal inversion of seismic surface wavefields, *Pure and App. Geophys.*, **163 (7)**.

Levshin, A.L., J. Schweitzer, C. Weidle, N. Shapiro, and M. Ritzwoller, 2006. Surface Wave Tomography of the Barents Sea and Surrounding Regions, submitted to **Geophys. J. Int.**.

Marquering, H., Snieder, R., & Nolet, G., 1996. Waveform inversions and the significance of surface mode coupling, *Geophys. J. Intl'*, **124**, 258-270.

Masters, G., Johnson, S. Laske, G., & Bolton, H., 1996. A shear-velocity model of the mantle, *Phil. Trans. R. Soc. Lond. A.*, **354**, 1385-1411.

McEvilly, T.V., 1998. Central U.S. crust - upper mantle structure from Love and Rayleigh wave phase velocity inversion, *Bull. Seism. Soc. Am.*, **54**, 1997-2015.

Mégnin, C. & Romanowicz, B., 2000. The three-dimensional shear velocity structure of the mantle from the inversion of body, surface and higher-mode waveforms, *Geophys. J. Intl'*, **143**, 709-728.

Mitchell, B.J., 1984. On the inversion of Love- and Rayleigh-wave dispersion and implications for the Earth structure and anisotropy, *Geophys. J. R. astr. Soc.*, **76**, 233-241.

Montagner, J.-P., 1994. Can seismology tell us anything about convection in the mantle?, *Rev. Geoph.* **32**, 115-137.

Montagner, J.-P., 1998. Where can seismic anisotropy be observed in the Earth's mantle? In boundary layers ..., *Pure and Appl. Geoph.*, **151**, 223-256.

Montagner, J.-P. & Anderson, D.L., 1989. Constrained reference mantle model, *Phys. Earth. Planet. Inter.* **58**, 205-227.

Montagner, J.-P. & Jobert, N., 1988. Vectorial tomography. II: Application to the Indian Ocean, *Geophys. J. R. astr. Soc.*, **94**, 309-344.

Montagner, J.-P. & Tanimoto, T., 1991. Global upper mantle tomography of seismic velocities and anisotropies, *J. Geophys. Res.*, **96**, 20,337-30,351.

Montagner, J.-P. & Kennett, B.L.N., 1996. How to reconcile body-wave and normal-mode reference earth models, *Geophys. J. Intl'*, **125**, 229-248.

Mooney, W.D., Laske, G., & Masters, G., 1998. A global model at 5° × 5°, *J. Geophys. Res.*, **103**, 727-747.

Nataf, H.-C., Nakanishi, I., & Anderson, D.L., 1986. Measurements of mantle wave velocities and inversion for lateral heterogeneities an anisotropy, *J. Geophys. Res.*, **91**, 7261-7307.

Nolet, G., 1990. Partitioned wave-form inversion and 2-dimensional structure under the network of autonomously recording seismographs, *J. Geophys. Res.*, **95**, 8499-8512.

Nolet, G. 2008. A Breviary of Seismic Tomography: Imaging the Interior of the Earth and Sun. Cambridge Press.

Ritzwoller, M.H. & Levshin, A.L., 1998. Eurasian surface wave tomography: group velocities, *J. Geophys. Res.*, **103**, 4839-4878.

Ritzwoller, M.H., Levshin, A.L., Ratnikova, L.I., & Egorkin, A.A., 1998. Intermediate-period group velocity maps across Central Asia, Western China and parts of Middle East, *Geophys. J. Intl.*, **134**, 315-328.

Ritzwoller, M.H., Shapiro, N.M., Levshin, A.L., & Garret, M.L., 2001 Crustal and upper mantle structure beneath Antarctica and surrounding oceans, *J. Geophys. Res.*, **106**, 30645-30670.

Ritzwoller, M.H., N.M. Shapiro, M.P. Barmin, and A.L. Levshin, 2002a. Global surface wave diffraction tomography, *J. Geophys. Res.*, in press.

Ritzwoller, M.H., N.M. Shapiro, A.L. Levshin, E.A. Bergman, E.A. Engdahl, 2003. The ability of global models to locate regional events, J. Geoph. Res., 1 08(B7), 2353,doi:10.1029/2002JB0 2003.

Shapiro, N.M. and M.H. Ritzwoller, 2002. Monte Carlo inversion for a global shear velocity model of the crust and upper mantle, Geophys. J. Int., 151, 88-105.

Shapiro, N.M. M. Campillo, L. Stehly, and M.H. Ritzwoller, 2005. High resolution surface wave tomography from ambient seismic noise, **Science**, **307(5715)**, 1615-1618.

Smith, M.L. & Dahlen, F.A., 1973. The azimuthal dependence of Love- and Rayleigh-wave propagation in a slightly anisotropic medium, *J. Geophys. Res.*, **78**, 3321-3333.

Snieder, R., 1988. Large-scale waveform inversions of surface waves for lateral heterogeneities, *J. Geophys. Res.*, **93**, 12,055-12,065.

Spetzler, J., Trampert, J., & Snieder, R., 2001. Are we exceeding the limits of the great circle approximation in global surface wave tomography? *Geoph. Res. Let.*, **28**, 2341-2344.

Trampert, J. & Woodhouse, J.H., 1995. Global phase velocity maps of Love and Rayleigh waves between 40 and 150 s period, *Geophys. J. Intl'*, **122**, 675-690.

Trampert J. and J. Spetzler, 2006. Surface wave tomography: Finite-frequency effects lost in the null space, *Geophys. J. Int.*, **164**, 394-400.

Villaseñor, A., Ritzwoller, M.H., Levshin, A.L., Barmin, M.P., Engdahl, E.R., Spakman, W., & Trampert, J., 2001. Shear velocity structure of Central Eurasia from inversion of surface wave velocities, *Phys. Earth. Planet. Inter.*, **123**, 169-184.

Woodhouse, J. H., 1988. The calculation of the eigenfrequencies and eigenfunctions of the free oscillations of the Earth and the Sun, in: *Seismological Algorithms* (D. J. Doornbos, ed.), 321-370.

Woodhouse, J.H. & Dziewonski, A.M., 1984. Mapping the upper mantle: three dimensional modeling of Earth's structure by inversion of seismic waveforms, *J. Geophys. Res.*, **89**, 5953-5986.

Yang, X., S.R. Taylor and H.J. Patton (2004). The 20-S Rayleigh Wave Attenuation Tomography for Central and Southeastern Asia, J. Geophys. Res. 109, B12304, doi:10.1029/2004JB003193.

Yoshizawa, K. and B.L.N. Kennett, Determination of the influence zone for surface wave paths, *Geophys. J. Int.*, **149**, 439-452, 2002.

Zhang, Y.S. & Tanimoto, T., 1992. Ridges, hot spots, and their interaction as observed in seismic velocity maps, *Nature*, **355**, 45-49.

Zhang, Y.S. & Tanimoto, T., 1993. High-resolution global upper mantle structure and plate tectonics, *J. Geophys. Res.*, **98**, 9793-9823.

Zhou, Y., F.A. Dahlen, G. Nolet and G. Laske, 2005. Finite-frequency effects in global surface-wave tomography, *Geophys. J. Int.*, **163**, 1087-1111.

Zhou Y., G. Nolet, F. A. Dahlen, G. Laske, 2006. Global upper-mantle structure from finite-frequency surface-wave tomography, *J. Geophys. Res.*, **111**, B04304, doi:10.1029/2005JB003677.